OPEN ACCESS

Catalysis & Surface REVIEW

Advances in directional liquid transport on solid surfaces

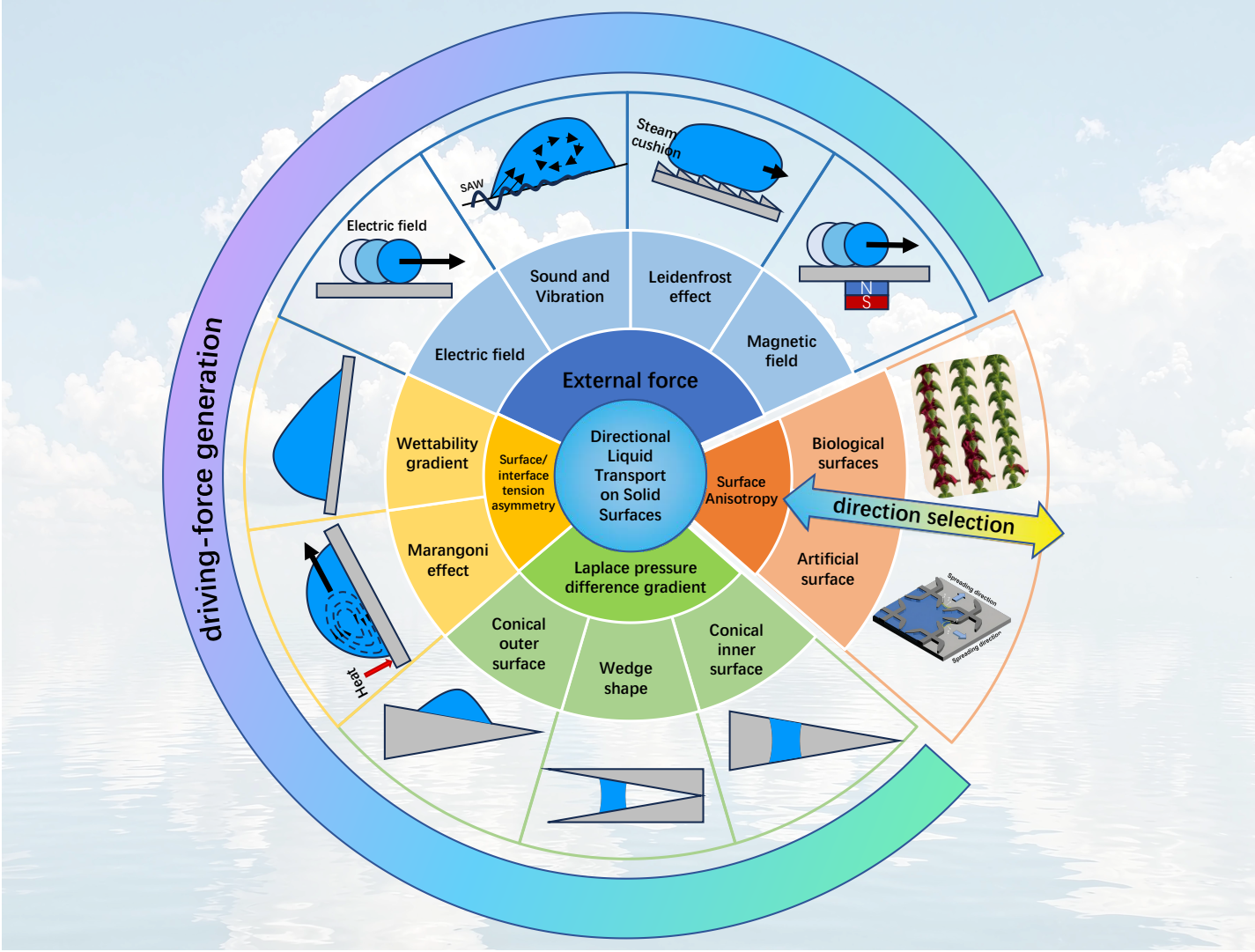
Yong Tian,[1,2] Xin Song,[1,2,*] Qianghui Xu,[3,*] Bingxiao Du,[1,2] Jialin Liang,[4] Zhenzhen Wang,[3] Yong Zhao,[1,2] and Jun Shen[3]

*Correspondence: songxin07@nudt.edu.cn(X. S.); xuqh12@bit.edu.cn(Q. X.)

Received: August 18, 2026; Accepted: October 19, 2026; Published Online: October 22, 2026; https://doi.org/10.59717/j.xinn-energy.2026.100200

© 2026 The Author(s). This is an open access article under the CC BY license (https://creativecommons.org/licenses/by/4.0/).

GRAPHICAL ABSTRACT



PUBLIC SUMMARY

- Directional liquid transport enables microfluidics, phase-change heat transfer, harvesting, and biosensing.
- This review links driving-force origin, force-transmission pathway, and directional-selection mechanism.
- Three driving pathways generate motion; anisotropic boundaries select its direction.
- Force direction, magnitude, and timescale govern reinforcement or opposition among mechanisms.
- Velocity-path maps guide task-oriented design through energy supply, resistance reduction, and rectification.

REVIEW Catalysis & Surface

OPEN ACCESS

www.the-innovation.org/the-innovation-energy

Advances in directional liquid transport on solid surfaces

Yong Tian,[1,2] Xin Song,[1,2,*] Qianghui Xu,[3,*] Bingxiao Du,[1,2] Jialin Liang,[4] Zhenzhen Wang,[3] Yong Zhao,[1,2] and Jun Shen[3]

[1]College of Aerospace Science and Engineering, National University of Defense Technology, Changsha 410073, China

[2]State Key Laboratory of Space System Operation and Control, Changsha 410073, China

[3]School of Mechanical Engineering, Beijing Institute of Technology, Beijing 100081, China

[4]Energy and Transportation Domain, Beijing Institute of Technology, Zhuhai, 519088, China

*Correspondence: songxin07@nudt.edu.cn(X. S.); xuqh12@bit.edu.cn(Q. X.)

Received: August 18, 2026; Accepted: October 19, 2026; Published Online: October 22, 2026; https://doi.org/10.59717/j.xinn-energy.2026.100200

© 2026 The Author(s). This is an open access article under the CC BY license (https://creativecommons.org/licenses/by/4.0/).

Citation: Tian Y., Song X., Xu Q., et al. (2026). Advances in directional liquid transport on solid surfaces. *The Innovation Energy* **3**:100200.

Directional liquid transport on solid surfaces underpins microfluidics, phase-change heat transfer, fog harvesting, and biomedical detection. Spatial asymmetry in interfacial properties, geometry, or external energy input generates a directional force. Contact-line pinning and opposing gravity set the onset condition, whereas viscous dissipation governs the transport rate. The conventional active–passive dichotomy distinguishes external power requirements but does not resolve the force-transmission pathway or the rectifying role of surface structure, particularly when several mechanisms coexist. This review therefore organizes directional transport at two complementary levels. The first distinguishes three pathways of driving-force generation: surface/interfacial-tension asymmetry, curvature-induced Laplace pressure gradients, and external-force actuation. The second addresses anisotropic rectification by solid surfaces, which sets direction-dependent boundary conditions and can operate with any of these driving pathways. Surface/interfacial-tension asymmetry comprises both wettability-induced contact-line force imbalance and Marangoni stress along liquid–gas or liquid–liquid interfaces. Chemical composition, roughness, and thermal, optical, electrical, and magnetic regulation are assessed, with particular attention to competition and cooperation between thermowetting and Marangoni stresses. Curvature-driven transport is traced from geometric confinement in wedges and cones to Laplace pressure gradients, biological prototypes, and optically or magnetically reconfigurable structures. Electric, magnetic, acoustic, vibrational, and Leidenfrost actuation are compared by energy input, force pathway, operating conditions, and limitations. Biological and engineered anisotropic surfaces are further interpreted as rectifiers that convert wetting, coalescence, or external excitation into direction-selective motion through asymmetric capillary advance and contact-line pinning. Cross-mechanism velocity–path comparisons identify operating windows and support task-oriented design through coordinated energy supply, resistance reduction, and rectification.

INTRODUCTION

Directional liquid transport on a solid surface denotes net liquid displacement along a prescribed direction under interfacial forces, pressure differences, gravity, or external energy input. Its defining requirement is not energy conversion alone, but spatial symmetry breaking in force, energy, or resistance. Motion starts when the directional driving force exceeds contact-line pinning and any opposing gravitational force; gravity may instead assist transport when aligned with the preferred direction. Viscous dissipation then governs the transport rate. Because interfacial effects become comparatively stronger at small scales, surface chemistry, micro/nanostructures, and external fields can reduce reliance on mechanical pumps and valves in miniaturized, integrated fluidic systems. These approaches support microfluidic manipulation,[1-3] fog harvesting,[4,5] heat-transfer enhancement,[6,7] biomedical detection,[8] and lab-on-a-chip platforms.

Most transport strategies have been organized around symmetry breaking and divided into passive and active methods.[9] Passive methods encode front–rear asymmetry through chemical modification or physical structuring without continuous external energy input. Wettability gradients,[10] structural gradients,[11] and anisotropic topologies[12] can thereby create surface/interfacial-tension asymmetry[13] or a Laplace pressure gradient within the liquid.[14] Their operating path and range, however, remain bounded by the prescribed gradient, available liquid volume, surface stability, and interfacial dissipation. Active methods use thermal,[15] optical,[16] electrical,[17] magnetic,[18] acoustic,[19] or vibrational[20] inputs to regulate the liquid or substrate. Such inputs enable dynamic control of direction, speed, and path, but impose additional requirements for power delivery, control, and device integration.

Recent reviews have approached directional liquid transport on solid surfaces from the perspectives of digital microfluidics, wetting anisotropy and gradient surfaces, functional superwetting surfaces, and bionic structured milli-fluidics (Table 1 and Supplementary Table S1). Their literature syntheses are organized around different target objects, classification criteria, and application aims, providing complementary foundations for structural design, actuation, and control. Building on this foundation, the present review examines how direct driving forces form and are transmitted in multimechanism systems, how surface structures select the direction of motion, and how condition-matched velocity–path records identify operating windows across mechanisms.

In terms of classification, structure- and morphology-oriented reviews help explain how geometric features influence droplet behavior, whereas reviews organized by driving mechanism or energy supply facilitate comparison among control strategies. Analysis of multimechanism systems further requires a common framework that distinguishes the energy source of the driving force, the force-transmission pathway, and the selective control exerted by the solid surface over the direction of motion.

Surface-structure classifications can intuitively reflect geometric effects on droplet behavior and are particularly useful for asking which configurations favour transport. The same structure may correspond to different direct driving forces under different wetting states or energy-supply conditions: for example, a conical structure can drive droplets through either a curvature-induced Laplace pressure gradient or a wettability gradient.[5] Structures can also establish a local pressure gradient, wettability gradient, or resistance asymmetry, or rectify an existing energy input into directional motion, as in vibration-assisted ratchet surfaces.[27] Accordingly, while retaining structural information, the present review further distinguishes direct driving force, force-transmission pathway, and rectification function.

The active–passive distinction clearly identifies whether a system depends on external energy input. When used as the sole classification dimension, the action pathway of an external stimulus and the directional-selection function of a surface structure still need to be considered separately. A single stimulus can activate several mechanisms, and a single transport event can combine several force contributions. A temperature gradient, for example, may alter substrate wettability[15] and simultaneously generate Marangoni stress along a liquid free surface;[28] the two effects can oppose or reinforce each other. Light may switch surface chemistry directly[29] or act through photothermal heating[30] and structural deformation.[31] A magnetic field may exert a body force on a responsive liquid[32] or reconfigure a substrate that subsequently couples wetting, gravity, or mechanical action to droplet motion.[33-35] Anisotropic structures introduce a different function: they are usually rectifiers rather than independent energy sources. Direction-dependent capillary advance, interfacial resistance, and contact-line pinning can convert wetting free energy, gravitational potential energy, coalescence-released surface energy, or external mechanical input into direction-selective motion. The present review therefore considers energy supply together with direct driving force, force-transmission pathway, and directional-selection function.

When mechanism selection and structural integration are considered, the respective roles of multiple effects and the comparability of performance information need to be examined within a common framework. Drop volume,

surface state, liquid-supply condition, and measurement method vary across studies; velocity and path data should therefore be interpreted under comparable conditions rather than used for a universal performance ranking. Accordingly, this review uses velocity–path records as a comparative dimension for operating windows and combines them with energy supply, resistance reduction, and rectification to discuss task-oriented design of mechanism combinations.

Based on these complementary perspectives, directional transport is classified here by the origin of the driving force and the mechanism of directional selection. Graphic abstract shows driving-force generation and directional selection in liquid transport on solid surfaces. Three driving pathways are distinguished: surface/interfacial-tension asymmetry, curvature-induced Laplace pressure gradients, and external-force actuation. Anisotropic solid-surface structures or wetting patterns provide directional guidance or rectification and can act in conjunction with any of these driving pathways.[36-37]

The framework distinguishes driving-force generation from directional selection. The first level comprises three driving pathways:

(1) Surface/interfacial-tension asymmetry. Spatial variation in substrate wettability creates a contact-line force imbalance, whereas a tension gradient along a liquid free surface or liquid–liquid interface generates Marangoni stress. The corresponding mechanisms are wettability-gradient actuation and the Marangoni effect.

(2) Curvature-induced Laplace pressure gradients. Geometric confinement imposes spatially unequal interfacial curvatures and establishes a pressure

Table 1. Review papers on directional liquid transport on solid surfaces

Reference	Year	Primary organizing dimension	Specific classification or scope	Main content	Review focus	Complementary perspective of the present review
Liu et al.[21]	2021	External-field type	Thermal, optical, electric and magnetic fields, and other stimuli	This review classifies field-induced droplet transport by stimulus type and systematically surveys thermal, optical, electric, and magnetic actuation together with other stimuli, and discusses how an external field generates an in-situ energy gradient, thereby overcoming the limitations of low transport speed and short transport distance associated with prefabricated surface gradients.	This review focuses on external-field-induced directional droplet transport, covering the fundamental wetting theory, the design of field-induced gradients, and applications in digital microfluidics, energy and water harvesting, heat transfer, and oil–water separation.	The present review treats the in-situ field-induced gradient as one of several origins of driving force and evaluates it against prefabricated interfacial gradients and curvature-induced Laplace pressure gradients through condition-matched velocity–path records.
Hou et al.[22]	2023	Gradient type	Chemical, roughness & curvature gradients	Based on natural biological surfaces, this work summarized three driving effects, namely chemical gradient, roughness gradient and curvature gradient, and discussed the corresponding action mechanisms under both droplet sliding mode and liquid spreading mode.	This review focuses on anisotropic gradient surfaces without external energy input and discusses the roles of chemical, roughness, and curvature gradients, including their combinations, in directional transport.	The present review places these gradients within a broader framework of driving-force origins and considers directional selection and cross-mechanism operating windows together with external-field inputs or interfacial energy released by droplet coalescence.
Li et al.[23]	2024	Dependence on external stimulus and driving force	Passive surfaces and active actuation	This review divides directional wetting surfaces into passive structures that require no continuous external power input and active surfaces driven by thermal, electric, magnetic, or optical stimuli.	This review focuses on the structure, working principles, and design methods of directional wetting surfaces, addresses surface-structure effects and emerging devices such as liquid diodes, and summarizes the mechanisms of external-field-driven directional liquid transport.	The present review adopts the direct origin of the driving force as the classification criterion and treats contact-angle hysteresis and pinning barriers as the resistance counterpart that determines whether a given driving force can produce net transport.
Bai et al.[24]	2025	Interfacial factor and transport strategy	Chemical composition, micro/nanostructure and macroscopic shape	This review organizes bioinspired fluid-manipulating interfaces along three interfacial factors, namely chemical composition at the molecular scale, micro/nanostructures that are more than ten times smaller than the droplet scale, and macroscopic shape comparable to the droplet scale, and discusses spontaneous transport and external-field-induced transport together with their applications.	This review focuses on bioinspired interfacial fluid manipulation and links the definition and classification of fluid-manipulating interfaces, regulation strategies based on special wettability and asymmetric structures, and applications such as fog and water harvesting, fluid diodes, interfacial catalysis, and microfluidics.	The present review maps these three interfacial factors onto driving-force origin, force-transmission pathway, and directional-selection function, and adds a condition-matched velocity–path comparison to identify operating windows relevant to different factor combinations.

Table 1. *(Continued)*

Reference	Year	Primary organizing dimension	Specific classification or scope	Main content	Review focus	Complementary perspective of the present review
Miao et al.[25]	2026	Manipulation strategy and energy supply	Passive surfaces, active manipulation, and active–passive hybrid systems	This review organizes intelligent liquid manipulation into three branches, namely passive surfaces designed on the basis of bioinspired structures and heterogeneous wettability, active manipulation driven by electrical, magnetic, optical, thermal, or acoustic stimuli, and hybrid systems in which a passive interface is programmed with external energy and the motion is then driven by the interfacial energy stored in the reconfigured surface.	This review focuses on hybrid strategies that combine the energy efficiency of passive surfaces with the adaptability of active control, and discusses bioinspired prototypes, fabrication routes, and applications in sustainable energy, thermal management, smart manufacturing, and medical engineering.	The present review resolves the "passive–active–hybrid" sequence into two complementary dimensions of energy-supply pathway and directional-selection mechanism, so that a hybrid system is compared with its passive and active counterparts through matched velocity–path records rather than being treated as a separate category.
Sun et al.[26]	2026	Transport dimensionality and structural hierarchy	1D trajectories, 2D planes and 3D spaces	This review classifies structure-enabled liquid manipulation by dimensionality, covering 1D trajectories for directional delivery along horizontal, vertically upward, and vertically downward paths, 2D planes for multidirectional transport and controlled wetting patterns, and 3D spaces for programmable transport and complex liquid–gas–solid interfaces.	This review focuses on structure-guided rather than external-field-driven liquid control, proceeds along bioinspired prototypes from Laplace pressure gradients to capillary effects, provides an in-depth analysis and summary of advanced liquid-manipulation mechanisms and methods according to transport dimensionality, and discusses the practical applications matched to them.	The present review treats dimensionality as a transport-path attribute rather than a classification axis, and places 1D, 2D, and 3D structures within one framework in which the same structure is assessed for the gradient it establishes, the resistance it sets, and the input it rectifies.
Xie et al.[9]	2026	Theory, manipulation mode & application	Theoretical basis, passive bionic transport, active manipulation & applications	This review is organized around theoretical foundations, passive liquid transport on bioinspired structures, active droplet manipulation by external stimuli, and cross-domain engineering applications.	This review addresses bionic structured milli-fluidics and systematically covers theoretical foundations, passive bioinspired structures, external-field strategies, mechanism–performance relationships, and cross-domain engineering applications.	The present review focuses on direct driving forces and structural rectification in directional liquid transport on solid surfaces and uses condition-matched velocity–path records to identify operating windows for mechanism combination and application matching.

gradient within a connected liquid. Wedges, conical outer surfaces, and conical capillaries are representative configurations.

(3) External-force actuation. Electrical, magnetic, acoustic, or vibrational input disturbs mechanical equilibrium through body forces, interfacial stresses, or direct mechanical action. Vapor-mediated actuation on a highly heated substrate, including the Leidenfrost effect, produces directional transport through vapor-film pressure, shear, and asymmetric boundary conditions. Thermal input may also enter the surface/interfacial-tension mechanisms described above by altering wettability or generating Marangoni stress.

The second level concerns how solid-surface anisotropy guides or rectifies liquid motion:

(4) Directional guidance and rectification by solid surfaces. Anisotropic structures or wetting patterns create direction-dependent conditions for capillary advance, contact-line pinning, and interfacial resistance. These conditions can guide liquid motion along preferred paths or produce liquid-diode-like rectification. The energy driving motion may originate from wetting, gravity, droplet coalescence, or external excitation. This directional-selection function can act in conjunction with any of the driving pathways in (1)–(3).

The following sections examine the physical basis, control variables, biological prototypes, engineered structures, operating conditions and limitations of each category. The two levels are complementary rather than parallel branches of a single-level taxonomy. A system may combine several Level I driving pathways with one or more Level II rectifying boundaries. By separating energy source, force-transmission pathway and directional-selection function, section 6 further uses condition-matched droplet velocity–path records to compare operating windows across mechanisms and translates multimechanism coupling into an energy-supply, resistance-reduction and rectification framework for mechanism selection, structural integration and application matching.

SURFACE/INTERFACIAL-TENSION ASYMMETRY

Surface/interfacial-tension asymmetry drives liquid motion by creating unequal capillary action along a contact line or tangential stress along a fluid interface. On a solid substrate, spatially varying wettability changes the local equilibrium contact angle and produces a contact-line force imbalance. On a liquid–gas or liquid–liquid interface, spatially varying surface/interfacial tension produces Marangoni stress and internal flow. These pathways must be distinguished because they act at different boundaries, even when the same thermal or compositional field generates both.

Surface tension can be expressed equivalently as the tangential force per

unit length of a liquid–gas boundary or as its free energy per unit area.[38] Interfacial tension extends this description to solid–liquid and liquid–liquid boundaries.[39] At equilibrium, the relevant tensions enter the contact-line force balance, while a uniform fluid interface has no tangential tension gradient. Spatial variation therefore generates either a resultant capillary force at the contact line or a tangential stress along the fluid interface.

Two mechanisms follow from this distinction.[22,40] A wettability gradient changes the solid–liquid and solid–gas interfacial-energy balance along the substrate, so the two ends of a droplet experience unequal contact-line forces. A surface/interfacial-tension gradient acts directly along a fluid interface and generates Marangoni stress that drives interfacial flow from lower toward higher tension. The resulting droplet migration still depends on the full force balance, including substrate wetting, pinning, gravity, and viscous dissipation.

Wettability gradients

A wettability gradient converts spatial variation in substrate affinity into a capillary-force imbalance at the three-phase contact line. The front and rear of a droplet then adopt different local contact angles, creating a net force toward the more wettable region. Motion begins only when this force exceeds the retention force associated with contact-angle hysteresis and contact-line pinning, together with any opposing gravitational force. Viscous resistance controls the ensuing migration rate.

A droplet commonly adopts a spherical-cap shape because liquid cohesion tends to reduce solid contact, whereas solid–liquid adhesion promotes spreading. The angle measured through the liquid between the liquid–gas interface and the solid is the contact angle. It ranges from 0° to 180° and characterizes the wetting state: angles below 90° indicate comparatively strong wetting and a lyophilic surface, whereas angles above 90° indicate weaker wetting and a lyophobic surface.[39]

For an ideal smooth and chemically homogeneous solid, Young's equation expresses the equilibrium force balance at the three-phase contact line:[41]

$$\gamma_{sg} - \gamma_{sl} = \gamma_{lg}\cos\theta \tag{1}$$

where γ_{sg}, γ_{sl}, and γ_{lg} are the solid–gas, solid–liquid, and liquid–gas interfacial tensions, respectively, and θ is the contact angle shown in Figure 1A.

Under a wettability gradient, the local equilibrium contact angle varies with position. Let the front of the droplet, denoted by A, lie on the more wettable region and the rear, denoted by B, lie on the less wettable region, such that $\theta_A < \theta_B$. The components of liquid–gas surface tension along the transport direction then fail to cancel around the three-phase contact line, producing a contact-line force imbalance F_γ[42] toward A. For an infinitesimal width dx normal to the transport direction, the corresponding force contribution is:

$$dF_\gamma = \gamma_{lg}(\cos\theta_A - \cos\theta_B)\,dx \tag{2}$$

Equation (2) represents the local thermodynamic driving contribution supplied by the wettability gradient, rather than the net force actually available for droplet motion. Here, γ_{lg} is the liquid–gas interfacial tension, θ_A and θ_B are the local equilibrium contact angles at A and B, respectively, and dx is the infinitesimal width normal to the transport direction. Because $\theta_A < \theta_B$, $\cos\theta_A - \cos\theta_B$ is positive. Integrating these projected contributions over the contact-line width gives the total driving force F_γ toward the more wettable region.

Surface roughness and chemical heterogeneity can trap the three-phase contact line in local metastable states, thereby producing contact-line pinning. The advancing contact angle θ_a is the critical apparent angle at which a stationary contact line begins to advance, whereas the receding contact angle θ_r is the critical angle at which it begins to recede. The static contact angle θ_e normally lies between these limits, such that $\theta_r < \theta_e < \theta_a$. Contact-angle hysteresis, represented by $\theta_a - \theta_r$, is the macroscopic manifestation of contact-line pinning; on an ideal smooth and chemically homogeneous surface, the three angles converge.[39] The two sets of angles have different roles. θ_A and θ_B are position-dependent local equilibrium angles that determine the wettability-gradient driving force, whereas θ_a and θ_r are dynamic thresholds for contact-line advance and recession and therefore characterize the retention force. Before the droplet can move, its leading and trailing contact lines must reach their respective local thresholds. The force F_γ generated by the wettability gradient must therefore exceed the pinning-induced retention force to produce net migration.[10] A wettability gradient is thus a prerequisite for this driving mechanism, but it is not sufficient to guarantee directional motion.

The maximum pinning-induced retention force $F_{pin,max}$ is commonly estimated from the critical sliding state on an inclined surface. When the substrate inclination reaches the critical sliding angle α_s, the downslope gravitational force equals the maximum retention force. The Furmidge relation[43] expresses this balance as:

$$\rho V_d g \sin\alpha_s = F_{pin,max} \approx C_F \gamma_{lg}(\cos\theta_r - \cos\theta_a)\,w \tag{3}$$

Here, ρ is the liquid density, V_d is the droplet volume, g is the gravitational acceleration, α_s is the critical sliding angle, w is the droplet contact width normal to the sliding direction, and C_F is the dimensionless Furmidge factor associated with droplet shape and contact-line geometry. Setting $C_F = 1$ gives the commonly used simplified form. Equation (3) uses the known gravitational force at incipient sliding to estimate $F_{pin,max}$. When the actual inclination exceeds α_s, the downslope gravitational component exceeds the pinning limit and the droplet slides downward.

For uphill, gravity-opposed migration on a surface inclined by α, take the uphill direction as positive. At incipient motion, the droplet velocity is zero and viscous resistance has not yet developed. The wettability-gradient driving force must therefore overcome both the maximum pinning-induced retention force and the downslope gravitational component:

$$F_\gamma > F_{pin,max} + \rho V_d g \sin\alpha \tag{4}$$

Equality defines the onset threshold; on a horizontal surface, $\alpha = 0$ and the criterion reduces to $F_\gamma > F_{pin,max}$. Once motion begins, the viscous resistance F_μ increases with velocity and enters the dynamic force balance. For uphill motion, this balance can be written as $F_\gamma - F_{CL,dyn} - \rho V_d g \sin\alpha - F_\mu = ma$. Here, $F_{CL,dyn}$ is the effective contact-line resistance during motion, and m and a are the droplet mass and acceleration, respectively. Under quasi-steady migration, $ma \approx 0$, and viscous resistance primarily determines the migration speed attained above the onset threshold. The wettability gradient therefore sets the preferred direction and available driving force, contact-line pinning and opposing gravity determine the onset condition, and viscous dissipation governs the subsequent transport rate.

A wettability gradient may be permanently encoded or dynamically generated.[44] Chemical gradients vary surface functional groups or composition;[10] roughness gradients change the apparent contact angle through micro/nanostructure.[45] Thermal,[15] optical,[29] electrical,[46] and magnetic[47] inputs instead regulate molecular configuration, phase state, interfacial charge, or substrate morphology. Despite different control variables, each route follows the same sequence: input or patterning changes local wettability, the front and rear contact angles become unequal, and a contact-line force imbalance drives motion once resistance is overcome.

Chemical Gradients. A chemical gradient varies the density or identity of surface functional groups and thereby changes the local solid–liquid and solid–gas interfacial energies.[39] Gradual variation in composition therefore produces a spatial contact-angle gradient and a corresponding contact-line force imbalance.[48-49]

In 1992, Chaudhury et al.[10] placed a clean silicon wafer 2 mm from a paraffin-oil solution of $Cl_3Si(CH_2)_9CH_3$. Vapor diffusion and surface reaction produced a hydrophobic region near the silane source while leaving the opposite end hydrophilic. The resulting front–rear wetting contrast directed the contact-line force toward the hydrophilic end. Water droplets consequently moved at approximately 1–2 mm s^{-1} and climbed a substrate inclined by about 15°, as shown in Figure 1D, after the capillary bias exceeded pinning and gravity.

The wetting asymmetry can also develop through reaction during spreading. Bain et al.[50] observed a decane droplet containing perfluorooctanoic acid moving uphill on a glass slide inclined by 43°. Decane wets clean glass, whereas the acid fluorinated the surface behind the droplet and suppressed subsequent spreading there. The unreacted region ahead remained more wettable, so the evolving chemical field biased motion forward. A prede-

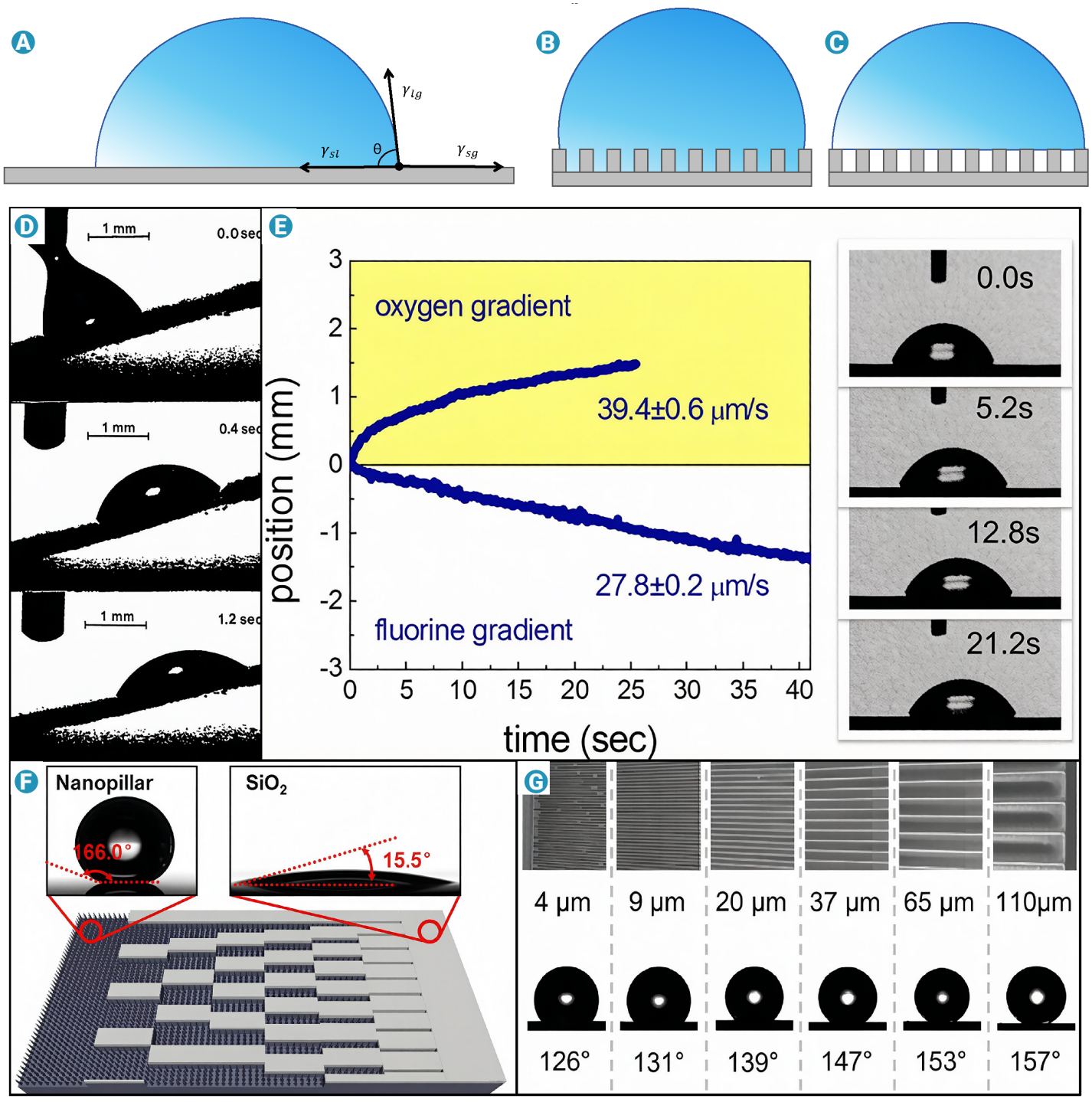


Figure 1. Young's equation and wetting configurations on rough surfaces and chemical gradients and roughness gradients that generate wettability gradients (A) Force balance underlying Young's equation. (B) Wenzel state. (C) Cassie–Baxter state. (D) A water droplet climbs against gravity under a chemical wettability gradient.[10] (E) Velocity profiles of H_2O droplets on oxygen (yellow) and fluorine gradient surfaces, with sequential images of H_2O droplet motion on an oxygen gradient.[13] (F) A discrete gradient formed by stepwise variation in the area fractions of superhydrophobic regions containing 3D nanoscale silicon pillars and hydrophilic SiO_2 planes.[45] (G) Contact angles in micropatterned regions with different groove dimensions.[51]

posited oleophobic film further confined spreading to one direction. This chemically coupled process is more specifically described as reactive spreading than as transport over a fixed gradient.

Electron-beam-generated plasma can create graded oxygen or fluorine functionalization on graphene and thereby impose a chemical wettability gradient.[13] Oxygen functional groups increase liquid affinity, driving water and dimethyl methylphosphonate toward regions of higher oxygen content. Fluorine functional groups lower surface energy, so both liquids move away from highly fluorinated regions toward lower fluorine content, as shown in Figure 1E.

A chemical gradient requires no continuous power after fabrication, but its spatial distribution and transport path are fixed. Organic contamination can alter the surface chemistry and weaken or erase the intended wettability contrast. Reconfiguring the path or direction therefore generally requires fabrication of a new gradient surface.

Roughness gradients. A roughness gradient changes apparent wettability without necessarily changing surface chemistry. Liquid may conform to the texture in the Wenzel state or rest on a composite solid–air interface in the

Cassie–Baxter state.[52-54] Spatial variation in roughness ratio, solid fraction, or wetting state then creates an apparent contact-angle gradient. The direction and magnitude of the resulting force depend on the intrinsic contact angle and on whether the liquid remains in one state or undergoes a Wenzel–Cassie transition.

In the Wenzel state shown in Figure 1B, liquid penetrates the surface texture and fully contacts the solid. The apparent contact angle is:

$$\cos\theta_w = r\frac{\gamma_{sg}-\gamma_{sl}}{\gamma_{lg}} = r\cos\theta \tag{5}$$

where θ_w is the apparent contact angle in the Wenzel state, θ is the contact angle on an ideal smooth surface of the same chemistry, and $r>1$ is the ratio of actual to projected solid area. Increasing r amplifies the intrinsic wetting tendency: a hydrophilic surface becomes more hydrophilic, whereas a hydrophobic surface becomes more hydrophobic.

In the Cassie–Baxter state shown in Figure 1C, the liquid rests on a composite interface of solid asperities and trapped air rather than filling the texture. The apparent contact angle is:

$$\cos\theta_c = f_1\cos\theta_1 + f_2\cos\theta_2 \tag{6}$$

where θ_c is the apparent contact angle of the composite surface. The intrinsic contact angles of materials 1 and 2, such as solid and air, are θ_1 and θ_2. The area fractions of materials 1 and 2 are f_1 and f_2, respectively, with $f_1+f_2=1$.

For a surface composed of several materials or interfacial fractions, the apparent contact angle can be written in the generalized Cassie form:[39]

$$\cos\theta_c = \sum_{i=1}^{N} f_i\cos\theta_i \tag{7}$$

where f_i and θ_i are the area fraction and intrinsic contact angle of component i, respectively, with $\sum f_i = 1$. For a two-component composite interface consisting of solid and trapped air, assigning the air contribution as $\cos\theta_{air} = -1$ reduces Equation (7) to the conventional Cassie–Baxter relation:

$$\cos\theta_c = f_1\cos\theta_1 - f_2 = f_1(\cos\theta_1+1)-1 \tag{8}$$

The reduced relation shows that a smaller solid fraction f_1 and a larger intrinsic solid contact angle θ_1 increase the apparent contact angle. The droplet is then supported more strongly by the trapped air layer and contacts less actual solid area.

Neither the Wenzel nor the Cassie–Baxter state is universally preferable; the appropriate state depends on the transported liquid form and operating conditions. For actuation by a contact-line force imbalance, the design objective is not to maximize the apparent contact angle alone, but to establish a sufficiently large front–rear $\Delta(\cos\theta_{app})$ while limiting contact-angle hysteresis and contact-line pinning and preserving wetting-state stability. In the Wenzel state, increasing the roughness factor r amplifies the intrinsic wetting tendency, making an intrinsically wetting surface more wetting and an intrinsically non-wetting surface less wetting. Complete impregnation of the texture, however, increases the actual solid–liquid contact area and often strengthens pinning, making this state more suitable for continuous spreading or capillary imbibition. In the Cassie–Baxter state, the apparent contact angle is regulated through the solid fraction. Reducing the solid fraction increases the apparent contact angle and decreases the actual solid–liquid contact area, which can favor low-resistance migration of discrete droplets when the composite state is stable. Its application therefore requires a stable trapped-air layer and control of the transition to the Wenzel state.

One implementation is to preserve the target wetting state while varying the microstructure or wetting-area fraction along the transport direction. The resulting continuous or discrete apparent-contact-angle gradient produces a front–rear contact-line force imbalance. Liu et al.[45] combined superhydrophobic regions composed of 3D nanoscale silicon pillars with hydrophilic SiO_2 planes and varied their area fractions stepwise along prescribed paths. The resulting discrete gradient spanned contact angles from 15.5° to 166.0°, as illustrated in Figure 1F, and directed droplets from high-angle to low-angle regions along circular and S-shaped paths. Decreasing the ratio of stripe length to droplet radius allowed each droplet to span more wetting units, increasing the front–rear apparent-contact-angle contrast and thereby increasing migration speed and transport distance.

A second implementation uses micropatterning to regulate the wetting-state transition while establishing a spatial wettability contrast. On the condenser surface reported in Ref.[51] the pattern promoted a Wenzel-to-Cassie–Baxter transition, reduced droplet adhesion, and formed a hydrophobic-to-hydrophilic gradient, as shown in Figure 1G. During dropwise condensation, droplets migrated from the hydrophobic end toward the hydrophilic end, promoting condensate removal and surface self-cleaning. This case shows how a controlled state transition can operate together with a wettability gradient, provided that the Cassie–Baxter state remains stable during condensation.

Compared with chemical gradients, structural gradients can offer greater wear resistance and stability. They are likewise difficult to reconfigure after fabrication, however, and their micro/nanostructures often require more complex and costly manufacturing.

Thermally Induced Wettability Gradients. Temperature can alter each term in Young's equation by changing solid–gas, solid–liquid, and liquid–gas interfacial tensions. A non-uniform substrate temperature can therefore generate a contact-angle field and a wettability-induced contact-line force imbalance. The same temperature field may also establish a liquid-surface-tension gradient, so thermowetting and thermal Marangoni stresses must be evaluated separately before assigning the migration direction.

Contact angle often decreases as temperature rises, but the response depends on the liquid, solid, and surrounding conditions.[55-58] For water, the measurements reviewed by Song and Fan[59] show only a slight decrease or near invariance in the low-temperature range at atmospheric pressure, generally below 100°C. Under pressurized conditions, more pronounced decreases were reported above about 120°C for some metallic substrates. Above about 210°C, the available data show a slowdown, an approximately constant contact angle, or a continued decrease. These ranges relate the contact-angle evolution to pressure, substrate material and roughness, the surrounding environment, and the measurement method, providing a reference for comparing measurements under different operating conditions.

Thermal input can generate a wettability gradient through four material pathways: polymer-chain conformation, localized photothermal heating, material phase transition, and surface-morphology reconstruction. Each pathway first changes the substrate state, then modifies local wettability, and finally creates a contact-line force imbalance. Whether the droplet migrates depends on pinning, gravity, and any simultaneous Marangoni stress.

Poly(N-isopropylacrylamide) (PNIPAAm) demonstrates conformational control.[15] Below 30°C, the grafted polymer surface is hydrophilic and exhibits high contact-angle hysteresis. Above 36°C, it becomes superhydrophobic with low hysteresis, while both contact angle and hysteresis vary markedly over 30–36°C. A temperature gradient across this transition writes a reconfigurable wetting contrast and directs droplet motion, as shown in Figure 2A. The polymer response sets the boundary condition; the immediate driving force is the resulting contact-line imbalance.

Photothermal heating can localize the same sequence without globally heating the substrate. In an Fe_3O_4–PDMS lubricant-infused surface, near-infrared irradiation creates a local hot region whose contact angle increases.[30] The resulting front–rear wetting contrast produces an asymmetric Young force and directional droplet motion, as illustrated in Figure 2B. Because illumination position and intensity set the temperature field, this optical-to-thermal pathway provides spatial control over the wettability gradient.

A phase-change interface provides another thermal control variable. Wang et al.[60] used graphene photothermal conversion to melt paraffin in a paraffin-infused porous graphene film (PIPGF), reducing the water contact angle from 102° to 79°. Combining this transition with a near-infrared mask created a programmable wetting contrast between illuminated and unilluminated regions. Droplets then followed the prescribed path in Figure 2C, linking optical patterning to thermal phase change and finally to a contact-line force imbalance.

Thermally activated shape recovery can instead modify roughness. Infrared heating restores the programmed morphology of shape-memory

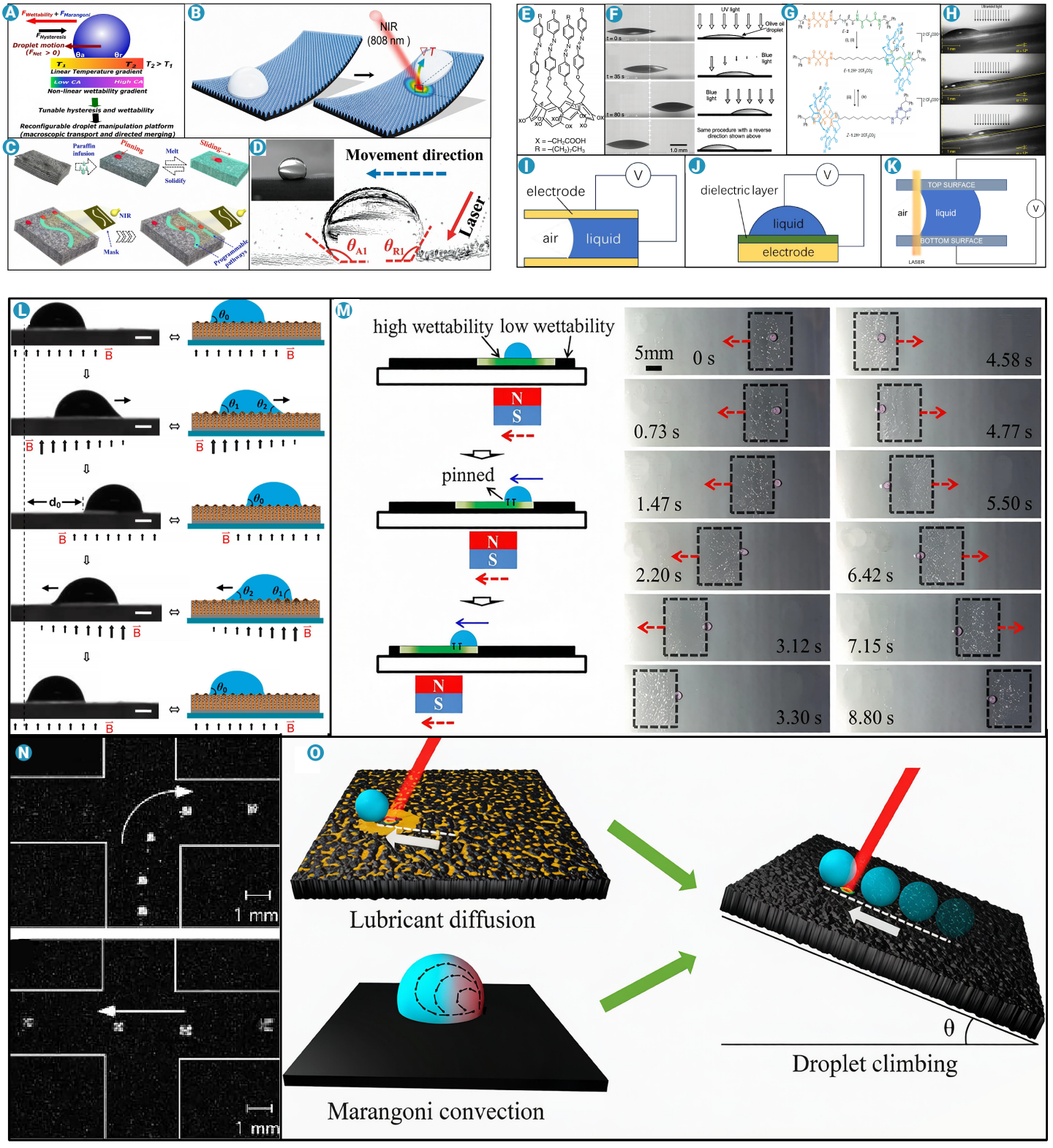


Figure 2. Directional liquid transport produced by thermally induced wettability gradients, photoinduced wettability gradients, electrically induced wettability gradients, magnetically induced wettability gradients, and Marangoni-driven droplet motion (A) A temperature gradient changes surface wettability through a molecular-chain conformational transition.[15] (B) Photothermal conversion creates a localized temperature field and a spatially addressable thermowetting gradient.[30] (C) A thermally induced phase transition changes interfacial wettability.[60] (D) Thermally triggered morphology change indirectly creates a wettability gradient.[31] (E) Macrocyclic amphiphiles bearing photochromic azobenzene units (CRA-CM).[29] (F) Light-driven motion of an olive-oil droplet on a CRA-CM-modified substrate.[29] (G) Synthesis and light-induced displacement of the macrocycle in a fluorinated molecular shuttle.[65] (H) A diiodomethane droplet moves against gravity on a 12° inclined mica surface modified with the molecular shuttle.[65] (I) Electrowetting (EW). (J) Electrowetting on dielectric (EWOD). (K)Optoelectrowetting (OEW). (L) A magnetic-field gradient reconfigures the substrate and transports a droplet along the induced wettability gradient.[47] (M) A moving magnetic field translates a high-wettability region that the droplet follows.[71] (N) Directional migration of a liquid-crystal droplet under a solutal Marangoni effect.[72] (O) Uphill droplet migration on an inclined surface under a photothermally induced Marangoni effect.[28]

micropillars and thereby changes their apparent wettability.[31] Spatial variation in the degree of recovery creates a morphology and contact-angle gradient that drives directional droplet motion, as shown in Figure 2D. In this pathway, temperature acts through geometry rather than directly through interfa-

cial chemistry.

These routes share the same force chain but differ in the substrate variable controlled by temperature: molecular conformation, local temperature, material phase, or surface morphology. Their force magnitude and preferred direction therefore need not be identical. A temperature field can also generate thermowetting and Marangoni contributions simultaneously.[61] Their combined force balance with contact-line pinning and gravity sets the migration direction, while viscous dissipation governs the speed.

Photoinduced Wettability Gradients. Light can alter wettability by switching molecular configuration, surface polarity, or exposed functional groups.[62,63] Spatially selective irradiation then creates a contact-angle field without direct mechanical contact. If the illuminated and unilluminated regions impose different local contact angles at opposite sides of a droplet, the resulting contact-line force imbalance drives migration once pinning and gravity are overcome.[64]

A photochromic azobenzene surface illustrates reversible chemical switching.[29] Figure 2E shows the tethered CRA-CM molecules. Ultraviolet light at 365 nm converts the azobenzene group from the trans to the more polar cis state, whereas 436 nm light restores the trans state and lowers wettability. Asymmetric blue-light exposure then maintains a lateral wetting contrast that transports an olive-oil droplet as the beam moves, as shown in Figure 2F. Under sustained liquid volume, reversible switching, and a movable light pattern, the actuation distance is set by the accessible illumination path rather than by a fixed pre-patterned gradient.

A light-driven molecular shuttle converts photoisomerization into controlled displacement of a molecular component.[65] The rotaxane E-1, synthesized from linear precursor E-2, contains fumaramide and tetrafluorosuccinamide stations, as illustrated in Figure 2G. Light converts fumaramide to the lower-affinity maleamide state, biasing Brownian motion of the macrocycle toward the tetrafluorosuccinamide station; subsequent treatment returns it. The displacement changes exposure of fluorinated groups and therefore surface wettability. This molecular event was sufficient to move a 1.25 μL diiodomethane droplet uphill against gravity on a 12° incline, as shown in Figure 2H.

Compared with thermally induced wettability gradients, photoinduced gradients can provide finer spatial addressability through the illumination position, wavelength, intensity, and intensity distribution. Local irradiation can write, erase, or translate the wetting field while reducing global heating and thermal diffusion, supporting reconfigurable paths and parallel droplet control. The operating boundary is set by photoswitch fatigue, response and recovery rates, optical penetration, and substrate optical properties. When photothermal heating is appreciable, it must be separated from direct photochemical switching because the associated temperature field can also generate thermowetting and Marangoni stresses.

Electrically Induced Wettability Gradients. Electrical control changes interfacial energy by redistributing charge at an electrode–electrolyte interface. In the electrocapillary description, the interfacial tension γ varies with the electrode potential ϕ_e according to the interfacial charge density σ:

$$\frac{d\gamma}{d\phi_e} = -\sigma \tag{9}$$

Beni and Hackwood reported an electrowetting display in 1981, showing that an electrical potential difference applied across a solid–electrolyte interface can reversibly regulate its apparent wetting state, as illustrated in Figure 2I.[66] Their three-electrode experiment immersed a gold-coated silicon substrate at 45° to a depth of 3 mm in K_2SO_4 solution. Pulses from −0.5 to +0.25 V reversibly displaced the gold–electrolyte meniscus by approximately 0.5 mm, with an upward speed of about 10 μm ms^{-1} under cathodic bias. No oxide formation was detected on gold, and the repeatable response established the feasibility of low-voltage, rapid liquid actuation for display concepts.

To avoid direct contact between the conductive droplet and the metal electrode, electrowetting on dielectric (EWOD) places a dielectric insulating layer between them,[67] as illustrated in Figure 2J. The dielectric isolates the droplet from the metal electrode, while its surface chemistry sets the initial wetting state; the applied voltage acts on the wetting interface through capacitive coupling across the dielectric. This device architecture enables local electrode addressing to create a contact-angle asymmetry and transport droplets.

For an ideal EWOD interface, the voltage-dependent contact angle follows the Young–Lippmann relation:[68]

$$\cos\theta(V_{app}) = \cos\theta_0 + \frac{\varepsilon_r\varepsilon_0}{2\gamma_{lg}d}V_{app}^2 \tag{10}$$

Here, $\theta(V_{app})$ and θ_0 are the contact angles with and without the applied potential difference V_{app}, respectively. The dielectric is characterized by vacuum permittivity ε_0, relative permittivity ε_r, and thickness d, while γ_{lg} is the liquid–gas interfacial tension.[67] Voltage increases $\cos\theta$ and thus enhances apparent wettability within the regime where the ideal relation remains valid. Applying voltage only near one side of a droplet makes the electrowetting force asymmetric and drives the contact line toward the energized electrode.

Programmable electrode sequences convert the local electrowetting force into droplet operations. Cho et al.[17] sequentially activated electrodes beneath the forward meniscus to transport, split, and merge droplets. Cooney et al.[69] integrated the ground electrode between the substrate dielectric and hydrophobic layers, eliminating the top plate and an external ground wire and thereby simplifying the transport geometry. Optoelectrowetting replaces fixed addressing with light-defined virtual electrodes, as illustrated in Figure 2K: illumination changes the conductivity of hydrogenated amorphous silicon (a-Si:H), redistributes the local electric field, and triggers electrowetting.[70] The projected pattern can consequently transport and split droplets or address several droplets in parallel.

Electrowetting provides rapid, reversible, and electronically programmable control of individual droplets. Its practical envelope is set by device complexity, electrolysis in direct-contact designs, contact-angle saturation, and dielectric breakdown. In this mechanism, the electric field changes the wetting boundary and creates an asymmetric contact-line force; this pathway is distinct from dielectrophoretic body forces acting directly on the liquid, which are discussed in Section 4.1.

Magnetically Induced Wettability Gradients. A magnetic field can regulate a nonmagnetic droplet indirectly by reconfiguring a magnetoresponsive substrate. Particle displacement, deformation, or fluid redistribution changes local roughness or interfacial composition, which changes apparent wettability and creates a contact-line force imbalance. The magnetic field is therefore the control input, while the immediate driving force on the droplet remains capillary rather than magnetic.

Two substrate designs illustrate this indirect pathway. In a magnetic-fluid/ZnO composite surface, a magnetic-field gradient switches the interface between rough and smooth states, producing a wettability gradient that transports a droplet[47] as shown in Figure 2L. In a lubricant-infused polymer containing magnetic particles and plasticizer, the applied field sharply increases local roughness and changes wettability, while removing the field nearly restores the initial state.[71] Because the wetting response varies with field strength, translating the field translates the high-wettability region, and the droplet follows through the associated contact-line force imbalance, as illustrated in Figure 2M.

Magnetic regulation can operate through opaque substrates and does not require photothermal conversion or patterned electrodes at the transport interface. These features may benefit enclosed or optically inaccessible configurations. Performance, however, depends on magnetic-field strength and gradient, substrate response time, deformation reversibility, and the stability of particles or lubricants. Any claim of biological compatibility must be established for the specific field, material, and exposure condition. Magnetic forces transmitted through responsive liquids, carriers or substrate deformation are discussed in Section 4.2.

Wettability-gradient strategies can thus be grouped by whether the spatial asymmetry is fixed in the surface or written dynamically by an external input. Chemical and roughness gradients offer passive operation but limited reconfigurability. Thermal, optical, electrical, and magnetic inputs can move or switch the wetting field, at the cost of power, control hardware, response-time constraints, and possible coupling to other forces. Across all routes, the control variable changes local wettability and unequal contact angles create a contact-line force imbalance. That force must exceed pinning and opposing gravity to initiate motion, whereas viscous resistance governs the transport

rate.

Marangoni effects

Wettability-gradient actuation in Section 2.1 is transmitted mainly through a contact-line force imbalance created by spatial variations in solid–liquid interfacial energy. The Marangoni effect instead arises from a surface- or interfacial-tension gradient along a liquid–gas or liquid–liquid interface. Spatial variations in solute concentration or temperature generate a tangential Marangoni stress, which drives interfacial flow from lower toward higher tension and establishes an internal circulation within the droplet.[40]

The origin of the tension gradient distinguishes solutal from thermal Marangoni effects. A solute-concentration gradient produces the solutal, or solutocapillary, effect, whereas a temperature gradient produces the thermal, or thermocapillary, effect; both may coexist in the same system.[73] In either case, the stress acts tangentially at the interface and is transmitted through the internal flow field, rather than acting primarily at the contact line. Practical control therefore relies on concentration gradients, localized heating or cooling, or photothermal conversion under localized irradiation.[73]

The "tears of wine" phenomenon illustrates solutal Marangoni flow.[39,73] Preferential evaporation of ethanol from a wine film on a glass wall enriches the upper region in water and raises its surface tension relative to the ethanol-rich film below. The resulting tangential stress draws liquid upward against gravity until the accumulated liquid becomes gravitationally unstable and drains down the wall as visible tears. This sequence links evaporation-induced composition change to a surface-tension gradient and macroscopic flow.

Electrochemical control provides an engineered route to solutal Marangoni actuation. Gallardo et al.[72] generated surfactant at one electrode and consumed it at the other, establishing a spatially non-uniform surfactant-concentration field in an organic liquid. Because the surfactant lowers local surface tension, this concentration field produced a tension gradient that directed the droplet along a prescribed path, as shown in Figure 2N. Unlike the evaporation-driven gradient in tears of wine, the electrochemical reactions actively set the solute distribution and hence the direction of actuation.

A temperature gradient can drive a droplet through two distinct interfacial pathways. For liquid–solid pairs in which contact angle decreases with temperature, the hotter region becomes more wettable and the resulting contact-line force points toward that region. For liquids whose free-surface tension decreases with temperature, the Marangoni stress drives interfacial flow from the hot side toward the cold side and contributes a coldward migration tendency. The centroid motion therefore follows the balance between thermowetting and thermocapillary contributions, rather than the temperature gradient alone.

The experiments of Brzoska et al.[61] resolved this competition through the wetting state. For strongly wetting droplets with small contact angles, the Marangoni contribution dominated and the droplet migrated toward the colder side. At larger contact angles, the thermowetting and Marangoni contributions became comparable and no pronounced migration direction emerged. Predicting thermally driven motion therefore requires both the temperature dependence of the contact angle and that of the liquid free-surface tension.

A thermoresponsive surface can reverse the thermowetting contribution and align it with the Marangoni contribution. The PNIPAAm-grafted structure[15] discussed in Section 2.1.3 is hydrophilic below 30°C and hydrophobic above 36°C. Under a temperature gradient, hot-side hydrophobization increases the local contact angle, producing a contact-line force toward the colder, more hydrophilic region. The lower free-surface tension on the hot side simultaneously produces a coldward Marangoni stress. Under the reported conditions, both contributions promote droplet migration toward the cold region, converting competition into cooperative actuation.

Photothermal conversion localizes the energy input and thereby improves spatial control of thermal Marangoni actuation. In the wrinkled composite film reported by Zhang et al. ,[28] the lubricant covered only part of the wrinkled structure, leaving the remainder exposed. Contact-line pinning immobilized the droplet without illumination. Irradiating the region behind the droplet converted optical energy into a local temperature gradient and the associated Marangoni stress, driving uphill migration against gravity on inclines exceeding 15°, as shown in Figure 2O. The induced thermocapillary flow also promoted lubricant redistribution within the wrinkles, reducing sliding resistance and enabling reversible switching between migration and pinning.

Marangoni actuation can deliver rapid droplet transport over comparatively long distances, but each means of generating the tension gradient introduces a different engineering constraint. Added solutes or surfactants can change droplet composition or cause contamination. In thermally driven systems, a thermowetting contribution that opposes the Marangoni contribution makes migration direction sensitive to their relative magnitudes, while global heating adds thermal diffusion and energy loss. Local photothermal control improves spatial selectivity but shifts the requirements to optical absorption, conversion efficiency, and material stability. Effective design therefore depends on controlling the surface-tension gradient while aligning it with, rather than against, other interfacial driving contributions.

CURVATURE-INDUCED LAPLACE-PRESSURE-GRADIENT ACTUATION

Chapter 2 focused on force asymmetry created through surface and interfacial properties. Here, geometry sets the curvatures of connected front and rear menisci. Each meniscus sustains a local Laplace pressure jump; unequal jumps at the two ends produce a capillary pressure difference and an internal pressure gradient. The resulting capillary force drives liquid from higher toward lower liquid-phase pressure when it exceeds hysteresis-induced contact-line pinning and any opposing gravitational force, while viscous resistance governs the transport rate. This mechanism does not require a spatial surface-chemistry gradient, but its performance still depends on wettability, contamination, and contact-angle hysteresis.

Surface tension sustains a pressure jump across a curved liquid interface. For a single interface, this local Laplace pressure jump is given by the Young–Laplace equation:[41]

$$\Delta p \equiv p_l - p_g = \gamma_{lg}\left(\frac{1}{R_1}+\frac{1}{R_2}\right) \tag{11}$$

Here, $\Delta p \equiv p_l - p_g$ is the liquid-to-gas pressure jump, γ_{lg} is the liquid–gas interfacial tension, and R_1 and R_2 are the two principal radii of curvature; $R_1, R_2 > 0$ for a liquid interface convex toward the gas.

A wettability gradient can affect both the contact line and the meniscus geometry. Selective coating inside a capillary produced the discontinuous wettability gradient studied by Weislogel.[74] When the front and rear menisci contacted regions of different wettability, they adopted different curvatures and hence different Laplace pressure jumps, establishing the internal pressure gradient shown in Figure 3A. The contact-line force imbalance and capillary pressure difference are therefore coupled manifestations of the same spatial variation in interfacial free energy, rather than necessarily independent forces.

A geometric gradient can impose the required curvature difference directly, without a spatial variation in surface chemistry. Variation of interfacial curvature along the transport direction creates unequal capillary pressures and drives spontaneous transport. Wedge-shaped[75] and conical[76] geometries provide representative configurations considered below.

Wedge-shaped structures

A wedge is a basic geometric capillary actuator because its local gap constrains the front and rear menisci to different curvatures. In a lyophilic wedge, the smaller radius of curvature at the narrow end corresponds to a lower liquid-phase pressure than at the wide end, so the resulting axial pressure gradient drives the droplet toward the narrowing gap. Both the pressure gradient and the capillary force vary with droplet position and local gap width. For a lyophobic wedge, the menisci can change from concave to convex, reversing the curvature sign and potentially the migration direction. Wedge geometry, contact angle, and contact-angle hysteresis must therefore be considered together.

The wedge mechanism was observed by Hauksbee in 1711: an oil droplet between two glass plates moved toward their narrowing junction and accelerated as the gap decreased.[75] Shorebirds use a dynamic version of the same geometry.[77] Cyclic opening and closing of the hydrophilic beak alternately advances and recedes the front and rear contact lines, while contact-angle hysteresis and the time-dependent wedge prevent the reciprocal motion from

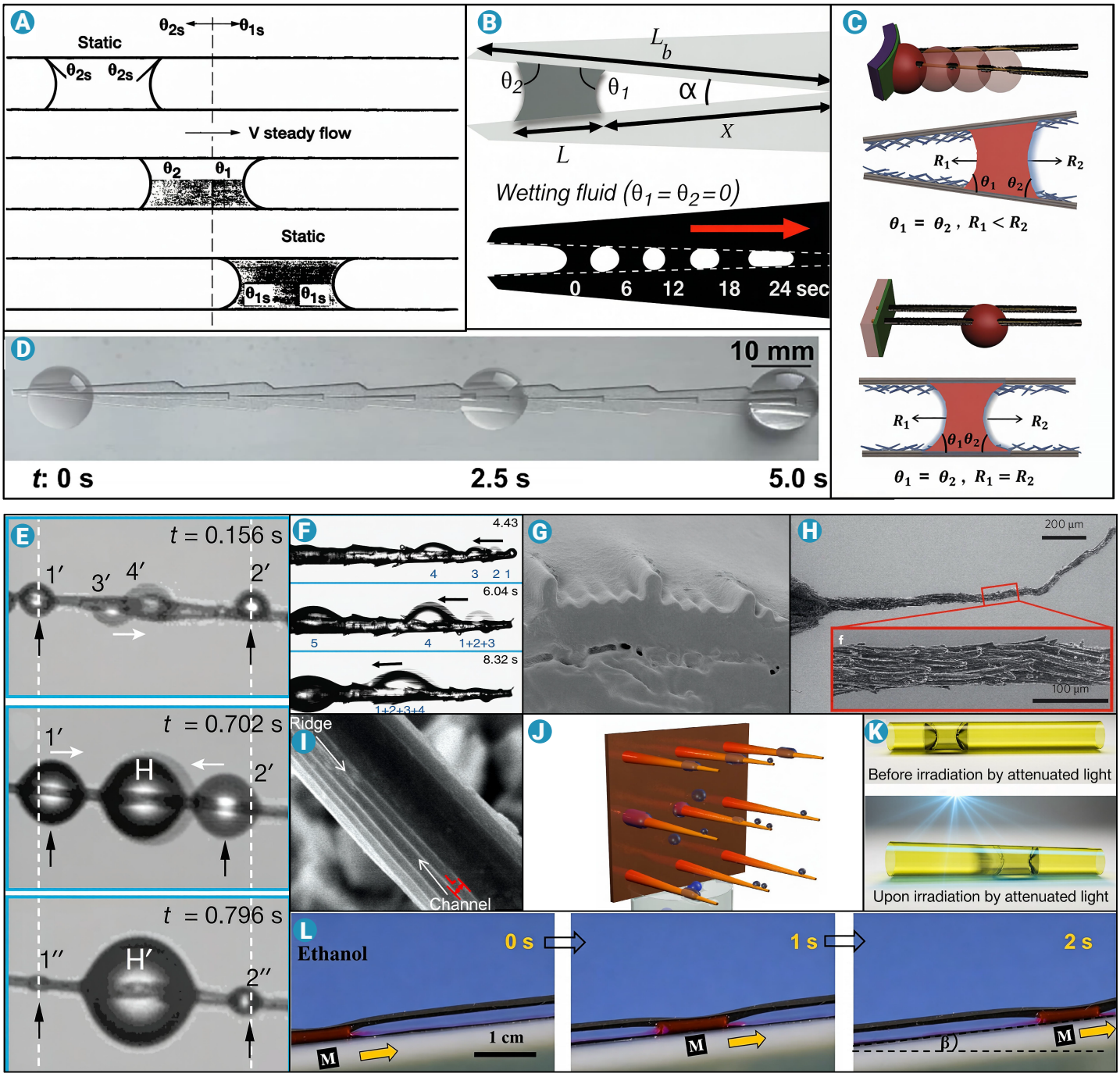


Figure 3. Laplace pressure gradients generated by wettability and wedge geometry, and curvature-induced capillary transport in conical geometries (A) Pressure gradient induced by a wettability gradient.[74] (B) Capillary-ratchet transport in a wedge-shaped shorebird beak.[77] (C) Droplet actuation by a bioinspired humidity-responsive wedge.[78] (D) Droplet actuation by a double-layer nested, segmented wedge.[78] (E) Droplet migration on wet-reconstructed spider silk.[81] (F) Droplet transport toward the base of a cactus spine.[82] (G) The surface of Sarracenia trichome features a hierarchical microchannel structure.[83] (H) The leaf awns of Syntrichia caninervis exhibit an overall conical structure with complex microstructures on the surface.[84] (I) The surface of scorpion setae features neatly arranged parallel channels and ridges, and these channels exhibit a gradient variation in width along the axial direction of the seta.[85] (J) Droplet actuation by coupled conical geometry and wettability gradients.[5] (K) Liquid transport in a photoinduced deformable capillary.[16] (L) Droplet transport in a magnetically deformable capillary.[87]

canceling. This capillary ratchet transports the droplet stepwise from the beak tip toward the mouth, as illustrated in Figure 3B.

A humidity-responsive device translates the wedge principle into switchable geometry.[78] The hydrogel, cellulose membrane, and superhydrophilic copper wires shown in Figure 3C unfold to form a wedge-shaped channel. The resulting front–rear curvature difference establishes a Laplace pressure gradient that moves the droplet toward the narrow end. When the wires return to a parallel arrangement, the curvature difference and capillary force decrease, and the droplet stops. Humidity therefore controls the geometry, whereas the reconfigured menisci provide the droplet-scale driving force.

The capillary force in a continuous wedge change with local gap and droplet position, which limits the useful travel distance. Li et al.[78] addressed this decay with a bamboo-inspired, double-layer segmented wedge. Different opening angles in the inner and outer layers re-establish a large curvature difference and accelerate the droplet within each unit. At a junction, the work performed by forward capillary traction, together with the incoming kinetic energy, must exceed the pinning barrier and hydrodynamic energy loss before the droplet can enter the next segment. Repetition of this process enables the cross-junction transport shown in Figure 3D, although the corresponding threshold remains to be quantified.

Two control variables can extend wedge actuation beyond a fixed geometry. Photoresponsive, thermoresponsive, or magnetoresponsive coatings can modify wettability; when this modification reduces contact-angle hysteresis while retaining sufficient capillary driving, the transport speed can increase. On a flexible substrate, external-field input can change the wedge angle and thereby regulate the Laplace pressure gradient, migration direction, and velocity in real time.

Conical external surfaces

An outer conical surface imposes a continuous axial variation in local radius and thereby confines droplet migration primarily to the cone axis. Because the front and rear contact regions occupy different radii, their interface curvatures and Laplace pressure jumps differ, creating an axial pressure gradient within the droplet. The resulting migration direction is set jointly by this curvature variation, the local taper, the wetting state, and contact-angle hysteresis.

Experiments on a conical wire showed that a completely wetting droplet migrates toward the region of larger local fiber radius and lower curvature, while the capillary driving weakens as that radius increases.[76] At constant droplet volume, the axial Laplace pressure gradient is expressed as

$$\frac{dp}{dz}\Big|_{\Omega} = -\frac{2\gamma_{lg}}{(r+h)^2}\left[\frac{dr}{dz}\Big|_{\Omega} + \frac{dh}{dz}\Big|_{\Omega}\right] \tag{12}$$

Here, p is the pressure inside the droplet, z is the axial coordinate measured from the cone tip, γ_{lg} is the liquid–gas interfacial tension, r is the local fiber radius, h is the maximum radial height of the free surface relative to the fiber axis, and Ω is the droplet volume; $d/dz|_{\Omega}$ denotes a total derivative along z at constant droplet volume.

The wetting state determines whether a droplet forms a barrel or clamshell morphology on the cone. A barrel-shaped droplet completely surrounds the fiber and is axisymmetric, allowing its migration to be described through a liquid-phase pressure balance. A clamshell-shaped droplet wets only part of the surface and has a three-dimensional asymmetric interface, so a front–rear pressure difference alone is insufficient to determine its motion. The barrel-droplet model in Ref.[80] incorporated a non-zero apparent contact angle, cone angle, surface microgrooves, and gravity to obtain the conditions for migration from the cone tip toward the base.

Spider silk[81] and cactus spines[82] illustrate how axial curvature gradients support fog collection and droplet migration. After wetting, spider silk reconstructs into alternating spindle-knots and joints; each spindle-knot can be approximated as two oppositely oriented cones joined at their bases. Unequal Laplace pressure jumps at the droplet interfaces then provide a capillary driving contribution from the joints toward the spindle-knots, as shown in Figure 3E. A cactus spine combines a conical profile with parallel grooves and an increasing diameter from tip to base. The associated curvature difference produces a base-directed Laplace pressure gradient and moves droplets from the tip toward the base, as shown in Figure 3F. In the reported experiment, the resulting capillary force exceeded the opposing gravitational and contact-line pinning forces even when the spine tip pointed vertically downward.

Beyond structures dominated by a conical curvature gradient, sarracenia trichomes,[83] syntrichia caninervis leaf awns,[84] and scorpion setae[85] couple axial grading with hierarchical channels, microbarbs, and liquid-film lubrication to integrate water capture, coalescence, and directional transport, as illustrated in Figure 3G-I. On sarracenia, water spreads rapidly through small hierarchical channels by capillarity and forms a precursor film, over which larger coalesced droplets subsequently slide with low resistance.[83] The syntrichia caninervis awn combines a conical profile, axial grooves, and microbarbs that facilitate condensation, fog interception, droplet coalescence, and delivery toward the leaf base.[84] Gradient channels on scorpion setae similarly promote microdroplet spreading and continuous-film formation, thereby reducing contact-line pinning and solid–liquid interfacial resistance during subsequent transport.[85] Together with spider silk and cactus spines, these examples show that directional water collection on biological surfaces commonly results from the coordinated action of geometric and wettability gradients, capillary spreading, and liquid-film lubrication, rather than from a curvature gradient alone. Conical profiles or axially varying channels establish curvature-dependent capillary pressure differences, roughness variations create apparent wettability gradients, hierarchical channels and microbarbs promote droplet capture and coalescence, and precursor films reduce contact-line pinning and solid–liquid interfacial resistance. Spider silk[81] and cactus spines[82] exhibit the same functional division: the conical geometry generates a Laplace pressure gradient, while roughness variations create a wettability gradient, with their coupling strengthening directional transport.[86]

This functional division provides a direct design rationale for engineered bioinspired surfaces. By controlling electrodeposition, Tang et al.[5] superimposed a chemical wettability gradient on the existing curvature gradient of conical copper needles. The curvature-induced Laplace pressure gradient and the wettability-induced contact-line force imbalance then acted in concert to improve droplet transport and fog collection, as shown in Figure 3J. The broader design lesson is not to reproduce biological morphology in its entirety, but to identify and integrate the structural and interfacial features required for droplet capture, directional driving, and resistance control.

The open geometry of an outer cone facilitates coupling with grooves and wettability gradients, but a single rigid cone retains two limitations: its curvature-induced pressure gradient decays along the transport path, and its axis fixes an essentially one-dimensional trajectory. Dynamic wettability control can modify the interfacial contribution, whereas serially connected conical units can restore a larger curvature difference in successive sections. These two strategies target transport strength and path length, respectively.

Conical internal surfaces

An axially varying tube diameter supports self-driven capillary transport within an enclosed geometry. A finite liquid slug forms front and rear menisci at different diameters, so their Laplace pressure jumps are unequal. The resulting capillary pressure difference establishes an axial pressure gradient within the liquid column. Relative to an outer conical surface, the enclosing wall provides continuous capillary confinement and reduces disturbances from evaporation and external airflow.

For a tapered capillary with uniformly wetting walls and stable, axisymmetric menisci at both ends of the liquid column, the Young–Laplace equation gives the capillary pressure difference Δp and the corresponding driving force F_D:[87]

$$\Delta p \approx \frac{4\gamma_{lg}\cos\theta}{\alpha x} - \frac{4\gamma_{lg}\cos\theta}{\alpha\,(x+\ell_d)} \approx \frac{4\gamma_{lg}\ell_d\cos\theta}{\alpha x^2}, \ell_d \ll x \tag{13}$$

$$F_D \approx \pi\alpha\gamma_{lg}\ell_d\cos\theta \tag{14}$$

Here, γ_{lg} is the liquid–gas interfacial tension, θ is the contact angle on the inner wall, and α is the small full apex angle of the cone in radians. The axial distance from the liquid-column front to the cone tip is x, and ℓ_d is the axial liquid-column length, with $\ell_d \ll x$. Under the small-angle approximation, the local tube radius is $R_{tube}(x) \approx \alpha x/2$. Equation (13) predicts that the capillary pressure difference decreases rapidly with distance from the cone tip, while the $\cos\theta$ term in Equation (14) sets the sign of the capillary driving force.

Static tapered-capillary experiments support these predictions. Renvoisé et al.[88] observed silicone oil, which completely wets glass, move spontaneously toward the tip of a lyophilic tapered tube. Liu et al.[89] likewise observed a wine droplet travel from the wide end toward the narrow end of a lyophilic glass capillary.

Unlike transport strategies that rely on two-dimensional geometric gradients, the "cellular fluidics" concept proposed by Dudukovic et al.[90] extends directional liquid manipulation from planar surfaces to three-dimensional open structures, where liquid flow is "programmed" through the architectural design of unit-cell type, size, and relative density. The physical basis of the directional transport is a curvature-induced Laplace pressure gradient: decreasing the strut diameter from inlet to outlet along the flow direction changes the effective pore size and hence the interfacial radius of curvature. The Young–Laplace relation then gives a higher pressure on the inlet side than on the outlet side, so the liquid advances spontaneously in the direction of decreasing pressure.

The same geometry that produces the capillary pressure difference also limits operation. Progressive narrowing toward the tip restricts sustained

throughput, while a fixed tube path precludes dynamic rerouting. After fabrication, contamination or material aging can change the wall wettability and increase contact-angle hysteresis and contact-line pinning, reducing the available capillary driving.

Photoresponsive deformation replaces a permanently tapered tube with an optically written diameter gradient. In the deformable capillary of Ref.[16], nonuniform 470 nm irradiation produced a local increase in cross-sectional area that grew with light intensity, converting an initially cylindrical microtube into an asymmetric, cone-like channel. The optical field supplied the control input for deformation; the resulting diameter gradient produced the capillary pressure difference that drove the liquid column toward the narrower end and along decreasing light intensity, as illustrated in Figure 3K. The same mechanism operated in straight, Y-shaped, serpentine, and helical capillaries, enabling transport along nonstraight paths.

A magnetoresponsive capillary uses the same separation between control input and liquid-scale force.[87] The applied field creates a local tapered deformation, whose unequal meniscus curvatures establish a Laplace pressure gradient and move the droplet toward the narrow end. Translating the magnet translates the deformed region, and the droplet follows with increasing velocity until the capillary can no longer respond rapidly enough to the moving field, as shown in Figure 3L. The magnetic field therefore reconfigures the tube, whereas the curvature-dependent capillary pressure drives the droplet.

Enclosed tapered capillaries combine continuous capillary confinement with reduced exposure to evaporation and external airflow, but their converging cross-section limits transport distance and throughput. Dynamic coupling to optical, magnetic, or other external-field inputs can move the active tapered region rather than forcing the liquid through a permanently narrowing channel. The attainable distance must then be balanced against the response efficiency and fatigue resistance of the deformable material.

Geometric curvature gradients do not intrinsically require spatial chemical patterning and may therefore offer a durability advantage, particularly for applications such as fog harvesting. Their principal limitation is that a single fixed gradient provides a decaying force over a finite distance. Coupling geometry with wettability gradients or multiscale structures, dynamically relocating the gradient with optical or magnetic inputs, and connecting segmented units address different aspects of this limitation. Engineering translation further requires reproducible fabrication, control of scale-dependent effects, and long-term operational stability in integrated micro- and nanofluidic devices.

EXTERNAL-FORCE ACTUATION

Chapters 2 and 3 classified mechanisms by the interfacial or capillary force that ultimately moves the liquid, even when thermal, optical, electrical, or magnetic inputs are used to create the required wettability or geometry. In those cases, the external field modifies an interfacial property or reconfigures a boundary, and the droplet-scale driving remains an interfacial-tension or capillary-pressure difference. External-force actuation follows a different pathway: externally supplied energy is converted into electric or magnetic force, acoustic radiation, inertial forcing, substrate-mediated mechanical action, or vapor-driven stress that acts directly or indirectly on the droplet and breaks its force or motion symmetry.

The external input allows rapid response, spatiotemporal control, and programmable paths in platforms such as digital microfluidics, but it also adds power, control, and integration requirements together with material-compatibility, biosafety, and reliability constraints. The following sections distinguish four energy-conversion pathways: electric-field forces,[91] magnetic forces,[18] acoustic fields[92] and substrate vibration,[93] and thermally sustained Leidenfrost actuation.[94]

Electric-field actuation

An external electric field polarizes a droplet and induces an effective dipole. An ideal uniform field can deform the droplet but produces no net translation because the forces on the two poles cancel. A non-uniform field couples the induced polarization to a field-strength gradient, leaving a net dielectrophoretic force $\mathbf{F}_{\mathrm{DEP}}$. For a nearly spherical or weakly deformed droplet in air whose dielectric response is described by real permittivities, the quasi-electrostatic dipole approximation gives:[95]

$$\mathbf{F}_{\mathrm{DEP}} = 2\pi\varepsilon_0 R_{\mathrm{d}}^3 \left(\frac{\varepsilon_{\mathrm{d}} - \varepsilon_0}{\varepsilon_{\mathrm{d}} + 2\varepsilon_0} \right) \nabla |\mathbf{E}_0|^2 \tag{15}$$

Here, ε_0 is the vacuum permittivity and approximates the permittivity of air, ε_{d} is the droplet permittivity, R_{d} is the droplet radius, and $\mathbf{E}_0$ is the local quasi-static field in the absence of the droplet. A positive polarization factor gives positive dielectrophoresis toward higher field strength, whereas a negative factor gives negative dielectrophoresis toward lower field strength.

Prefabricated coplanar electrodes provided an early means of creating non-uniform fields. Patterning the electrodes on an insulating substrate confined liquid to high-field regions and formed finger-like streams above the electrodes,[96,97] as shown in Figure 4A. Because the electrode geometry fixed the field distribution, it also fixed the available transport path and limited reconfiguration.

Reconfigurable field gradients remove the constraint of a fixed electrode path. A charged glass rod creates a movable non-uniform field that guides water droplets along a superhydrophobic track,[98] as illustrated in Figure 4B, although manual positioning limits automation. Surface charge printing provides a more integrable alternative: a rewritable charge-density gradient generates the local field that drives droplets toward higher charge density,[99] as shown in Figure 4C. Ionic wind erases the pattern, and processes such as droplet impact can write a new one, allowing the transport path to be reprogrammed.

Photoinduced charge generation replaces a written charge pattern with an optically addressable one. The near-infrared-responsive material in Ref.[100] generated localized surface charge during irradiation and allowed it to dissipate after the light was removed. Beam position, incidence angle, and intensity controlled the magnitude and direction of the dielectrophoretic force, enabling forward translation, backward translation, and rotation, as shown in Figure 4D. The movable light spot therefore supports complex trajectories and parallel droplet manipulation without a fixed electrode path.

Electrowetting, discussed in Chapter 2, and dielectrophoresis use the same electrical input but transmit it through different forces. Electrowetting-on-dielectric (EWOD) changes the effective wetting energy and apparent contact angle, so asymmetric actuation produces a contact-line force imbalance. Dielectrophoresis instead couples droplet polarization to a non-uniform field and produces a net electric force on the droplet.

Dielectrophoretic translation requires a stable and spatially controlled electric-field gradient rather than permanent chemical modification of the substrate. Prefabricated electrodes provide field stability but limited path reconfigurability; printed surface charges are rewritable but sensitive to environmental disturbance; and photoinduced charge systems are limited by attainable charge density, response time, and cycling stability. Combining stable photoelectric materials, addressable electrode arrays, and dynamic optical fields can support low-voltage, low-energy, parallel droplet manipulation.

Magnetic-field actuation

Magnetic fields provide remote, noncontact control through magnetoresponsive media, making them relevant to enclosed microchannels and biomedical microfluidics. Magnetically induced changes in wettability are discussed in Section 2.1.6; this section focuses on direct magnetic forces and mechanical transmission through a deformable substrate. The force-transmission pathway separates magnetic actuation into two classes. In direct actuation, a field gradient acts on a magnetoresponsive droplet or contacting carrier and transfers magnetic force to the target droplet. In indirect actuation, the field deforms the substrate, and the resulting gravitational potential well or mechanical thrust transports a nonmagnetic droplet.

Direct magnetic-force actuation. Direct magnetic actuation requires a magnetoresponsive unit that remains mechanically coupled to the target droplet. The unit can be formed by particles dispersed within the droplet or by a contacting but distinct ferrofluid, magnetic liquid metal, or solid carrier. Although this approach reduces the need for patterned substrate microstructures, its performance is set by the magnetic-field gradient, effective susceptibility of the responsive unit, and interfacial coupling through which force is transmitted to the droplet.

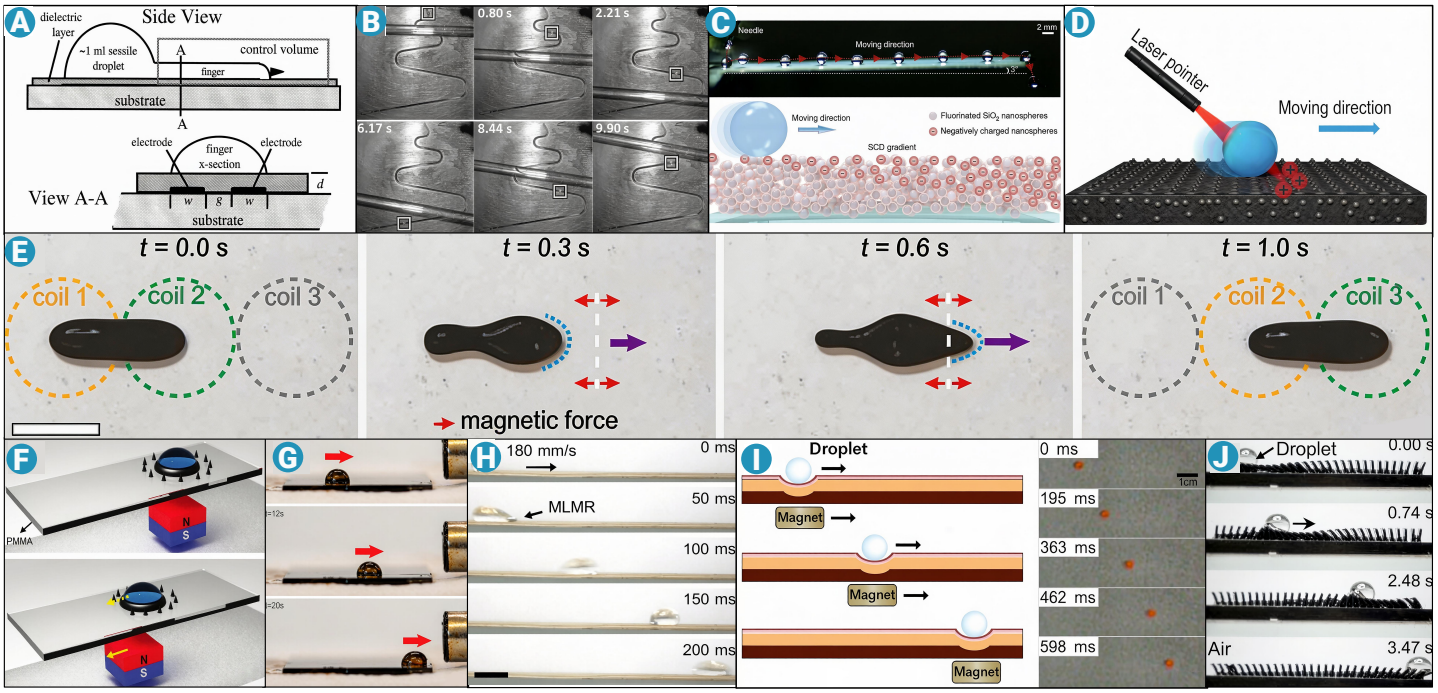


Figure 4. Directional liquid and droplet actuation by electric-field and magnetic-field forces (A) Patterned electrodes confine liquid in high-field regions and form finger-like streams.[96] (B) A charged glass rod generates a non-uniform field that guides a droplet along a superhydrophobic track.[98] (C) A surface-charge-density gradient drives droplet migration.[99] (D) Photoinduced charge generation enables programmable droplet actuation.[100] (E) Ferrofluid-droplet migration in a magnetic field.[101] (F) Transport by a field-controlled ferrofluid ring.[32] (G) Transport of a ferrofluid-encapsulated droplet.[102] (H) Mechanical transport by a magnetic liquid-metal robot (MLMR).[18] (I) Droplet transport through a magnetically reconfigured gravitational potential well.[35] (J) Mechanical actuation by a magnetoresponsive microplate array.[33]

Ferrofluids are stable colloidal suspensions of magnetic nanoparticles in an oil- or water-based carrier fluid.[32] Surfactant modification suppresses particle aggregation and supports long-term dispersion stability.[101] For a linear, isotropic magnetic response below magnetic saturation, the magnetic force $\mathbf{F}_m$ on the responsive droplet can be approximated as:[103,104]

$$\mathbf{F}_m = \frac{V_d \chi}{\mu_0 (1+\chi)} (\mathbf{B} \cdot \nabla) \mathbf{B} \tag{16}$$

Here, V_d is the magnetoresponsive droplet volume, χ is the volume magnetic susceptibility of the responsive droplet or liquid phase, μ_0 is the vacuum permeability, and $\mathbf{B}$ is the magnetic flux density at the droplet position. A uniform field primarily produces magnetization and deformation, whereas a spatial field gradient drives net translation. Field design can therefore control both ferrofluid deformation and directional migration,[101] as illustrated in Figure 4E.

Under an out-of-plane magnetic field, Nasirimarekani et al.[32] observed an ordered spike pattern in an oil-based ferrofluid and a ferrofluid ring around the base of a water droplet. For the material used in that study, droplet height varied with field strength up to magnetization saturation near 90 mT, and spikes appeared when the field was increased further. This field-driven morphological evolution established the operating configuration for ring-mediated manipulation at the liquid–liquid interface. When water contacted the spike pattern, liquid–liquid interfacial interaction formed a ring around the droplet base; translating the external magnetic field moved both the ring and the coupled droplet, as shown in Figure 4F. In a related configuration, an oil-based ferrofluid impregnates a micropillar array[102] and spreads over a water droplet in contact with the surface to form an encapsulating film. A lateral field gradient drives the encapsulated droplet toward higher field strength, while a moving subsurface magnet guides its motion, as shown in Figure 4G.

Magnetoresponsive liquid-metal and solid carriers provide two further means of transmitting magnetic force, with the liquid-metal force taking the same general form as that for a ferrofluid.[103,104] The reconfigurable magnetic liquid-metal robot (MLMR) in Ref.[18] combined iron nanoparticles with a hydrophilic gallium–indium–tin alloy. On a superhydrophobic surface, the MLMR followed a moving magnet and transmitted force to an attached droplet through liquid–gas interfacial confinement and contact-line adhesion. In the condition reported in Ref.[18], an MLMR of diameter about 1.1 mm and volume about 0.70 μL transported a droplet of about 1100 μL at 5 mms^{-1}, corresponding to a volume ratio of about 1571, as illustrated in Figure 4H. A pair of hydrophilic steel beads provides a solid-carrier alternative for programmable droplet transport and related operations.[105]

The principal boundary for direct magnetic actuation is material contact with the target liquid. Dispersed magnetic particles can alter composition and deposit within microchannels. Ferrofluid encapsulation and separate carriers reduce bulk modification, but carrier–droplet mass transfer, residues, and cross-contamination remain possible. Applications such as drug delivery or high-purity reagent transport therefore require evaluation of the specific interface and material-safety requirements, despite the advantages of remote control and limited substrate patterning.

Indirect magnetic actuation. Indirect magnetic actuation separates the magnetoresponsive component from the target liquid. The field reversibly deforms the substrate, and the deformed structure transports a nonmagnetic droplet through a moving gravitational potential well or mechanical thrust. Because the liquid requires no magnetic additive, the same force-transmission concept can be applied to water, organic solvents, and other droplets.

The magnetoelastic plate in Ref.[35] converts magnetic input into a moving gravitational potential well. An approaching magnet forms a local concave bowl in the superhydrophobic surface, gravity moves the droplet to its lowest point, and translation of the magnet carries both the bowl and droplet, as shown in Figure 4I. Magnetoresponsive cilia and microplate arrays use a different transfer path: reversible field-induced deformation generates mechanical thrust, assisted where applicable by gravity, to drive directional motion,[33,34] as shown in Figure 4J. A rotatable-blade array similarly converts magnetic actuation into direct mechanical pushing for continuous droplet transport.[106]

Mechanical relaxation sets the dynamic limit of indirect magnetic actuation. If substrate deformation lags the moving field, the structure cannot sustain high-speed transport; repeated deformation can also accumulate fatigue damage. Response time and cyclic durability therefore determine the attainable operating speed and long-term stability.

Sound and vibration

Acoustic fields and substrate vibration both introduce mechanical energy, but they deliver momentum to a droplet through different routes. Acoustic-field actuation transmits momentum through wave propagation and attenuation in the liquid or surrounding medium, allowing contactless manipulation at the cost of transducer, field-control, and calibration requirements. Substrate vibration transfers momentum directly from the accelerating solid to droplet inertia, deformation, and contact-line motion. Its directionality can be tuned through the vibration mode, but this same dependence makes transport sensitive to modal design.

The two categories are therefore distinguished by the dominant momentum-transfer pathway rather than by the excitation source alone. In acoustic-field actuation, nonlinear momentum transfer generates acoustic streaming. A non-uniform acoustic field can also exert a radiation force and establish an acoustic potential trap. In substrate-vibration actuation, solid acceleration acts through inertia, interfacial deformation, and nonlinear contact-line dynamics. Surface acoustic-wave devices and ultrasonically excited substrates can contain both pathways, with their relative importance set by device architecture, vibration mode, and wetting state.

Acoustic-field actuation. Acoustic-field actuation uses a contactless or low-contact acoustic wave as the energy carrier. It avoids physicochemical modification of the target droplet and reduces mechanical-contact-related contamination. The subsequent analysis separates hydrodynamic forcing by acoustic streaming from time-averaged acoustic radiation forcing and acoustic potential trapping.

Acoustofluidic devices are commonly classified as bulk acoustic-wave (BAW) or surface acoustic-wave (SAW) systems according to the transducer mode.[3] When a SAW couples to a surface liquid, part of the acoustic energy enters the liquid as a leaky wave and is attenuated by viscosity. The resulting nonlinear, time-averaged momentum transfer generates steady acoustic streaming within the droplet or surrounding medium. Spatial asymmetry in the acoustic or streaming field then produces a net hydrodynamic force and droplet migration,[92] as illustrated in Figure 5A. This pathway has been used to regulate flow and heat transfer in continuous microchannels[107] and drive droplet spreading and directional migration.[108] It has also created hydrodynamic traps for droplet transport, mixing, and coalescence.[109]

A non-uniform acoustic field can also act on a droplet through acoustic radiation pressure rather than through streaming drag. For a periodic steady field, the acoustic radiation force is the second-order, time-averaged result of wave–droplet interaction. If viscous shear is neglected and the acoustic action is represented by the normal radiation-pressure distribution over the droplet interface, the time-averaged radiation force $\mathbf{F}_{rad}$ is:[110]

$$\mathbf{F}_{rad} = -\int_{S_0} \langle p_{rad} \rangle \mathbf{n} dS \tag{17}$$

Here, S_0 is the droplet interface, $\mathbf{n}$ is the outward unit normal from the droplet into air, and $\langle p_{rad} \rangle$ is the time-averaged acoustic radiation pressure on that interface. For a small-amplitude, periodic steady, approximately inviscid acoustic field in air, this pressure is:[111]

$$\langle p_{rad} \rangle = \frac{\langle p_1^2 \rangle}{2\rho_0 c_0^2} - \frac{\rho_0}{2} \langle |\mathbf{v}_1|^2 \rangle \tag{18}$$

Here, ρ_0 and c_0 are the equilibrium density and speed of sound in air, respectively, while p_1 and $\mathbf{v}_1$ denote the first-order acoustic-pressure perturbation and acoustic particle velocity; $\langle \cdot \rangle$ denotes averaging over one acoustic period.

Standing waves form periodic pressure nodes and antinodes. In the droplet–air systems considered here, acoustic radiation forces generally move droplets toward pressure nodes. Properly configured three-dimensional standing, focused, or phased-array fields can create an acoustic potential minimum that balances gravity and confines lateral motion,[112] as shown in Figure 5B. Moving this potential trap enables acoustic-tweezer transport, capture, and positioning on a surface or in free space.[19] This radiation-force pathway differs from the hydrodynamic trapping reported by Zhang et al.[109] There, interdigital transducers excite bulk and leaky surface acoustic waves in a fluorinated-oil carrier, and acoustic streaming transports floating droplets by viscous drag toward hydrodynamic equilibrium positions. Sequential activation of the traps then guides the droplets along prescribed paths, as shown in Figure 5C.

The operating boundary of acoustic-field actuation is set by the required control dimensionality. Single-transducer and simple SAW devices can provide relatively direct contactless or low-contact manipulation, whereas multidroplet, three-dimensional, and complex-trajectory operation requires phase control, transducer-array calibration, and feedback positioning. Increasing programmability therefore raises the demands on device integration and field control.

Solid-substrate-vibration actuation. In substrate-vibration actuation, mechanical energy enters through the accelerating solid and is transferred directly to droplet inertia, interfacial deformation, and contact-line motion. Directional migration requires this periodic response to become asymmetric over a vibration cycle. Vibration direction, mode, frequency, amplitude, and phase can provide that directional selection. The device can be simpler than a spatial acoustic-trapping system, but the force balance and migration direction remain sensitive to mode shape, resonance, and amplitude distribution.

Standing substrate modes provide a representative route for vibration control. Wu et al.[93] ultrasonically excited a circular 6061-aluminum-alloy plate and measured a radial vibration-velocity gradient with concentric nodal and antinodal lines. Droplets migrated along the increasing-velocity direction towards an antinode and remained there, as illustrated in Figure 5D. In that experiment, acoustic radiation pressure induced droplet deformation, contact-angle change, and internal flow, while high-frequency vibration also generated viscous momentum transfer near the contact line at the solid–liquid interface. The vibration-velocity gradient produced unequal effective actions at the front and rear of the droplet; these actions approached balance near the antinode, where the droplet remained trapped.

To describe the local contact-line response under high-frequency vibration, the combined effect of acoustic radiation pressure and near-contact-line momentum transfer is represented by the radial acoustic line force f_{ac} per unit contact-line length. The local balance at the front three-phase line is

$$f_{ac} = \gamma_{lg}\cos\theta + \gamma_{sl} - \gamma_{sg} = \gamma_{lg}(\cos\theta - \cos\theta_0) \tag{19}$$

Here, γ_{lg}, γ_{sl}, and γ_{sg} are the liquid–gas, solid–liquid, and solid–gas interfacial tensions, respectively, and θ is the dynamic front contact angle. The second equality in Equation (19) assumes that the three interfacial tensions remain unchanged during vibration and uses the initial Young balance $\gamma_{sg} - \gamma_{sl} = \gamma_{lg}\cos\theta_0$. The viscous penetration depth is $\delta_v = \sqrt{2\mu/(\rho\omega)}$, where μ, ρ, and ω are the liquid dynamic viscosity, density, and vibration angular frequency. With U_a denoting the substrate vibration-velocity amplitude and R_c the droplet contact radius, the radial acoustic line force per unit length is approximated by

$$f_{ac} \approx \frac{\rho}{32\delta_v}(U_a R_c)^2 \cos^2\theta, \delta_v = \sqrt{\frac{2\mu}{\rho\omega}} \tag{20}$$

Substituting Equation (20) into the contact-line balance above gives

$$\cos\theta - \cos\theta_0 = We\frac{R_c}{\delta_v}\frac{\cos^2\theta}{32}, We = \frac{\rho U_a^2 R_c}{\gamma_{lg}} \tag{21}$$

Here, θ_0 is the initial front contact angle and $We = \rho U_a^2 R_c/\gamma_{lg}$ is the Weber number based on substrate vibration-velocity amplitude and contact radius. At fixed liquid properties and vibration frequency, $\rho/(32\delta_v)$ is constant, so Equation (20) can be used to compare the acoustic line force as vibration intensity changes; Equation (21) gives the corresponding dimensionless contact-angle response. Its use across frequencies, mode shapes, or geometries requires the corresponding U_a field and contact-line state. In a standing mode with a spatial vibration-velocity gradient, the local actions and their directions at the front and rear contact lines together produce antinode-directed migration; the opposing actions approach balance near the antinode.

The antinode-directed regime is recovered when acoustic radiation pressure is the dominant droplet-scale force. A standing wave of sufficient amplitude then moves a droplet toward the adjacent substrate-vibration antinode.[116] Switching the beam mode relocates that antinode and enables stepwise transport along the structure.[117] Directional selection is therefore

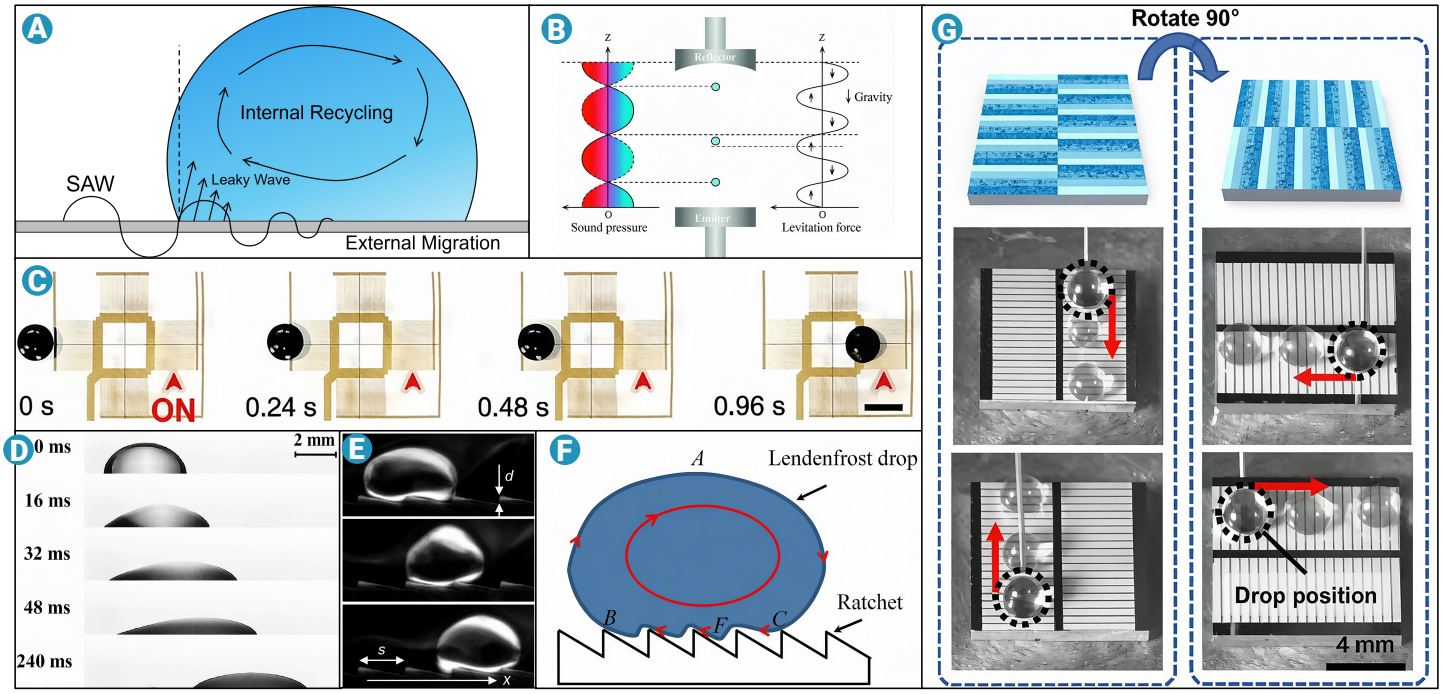


Figure 5. Droplet motion driven by sound and vibration, and by the Leidenfrost effect (A) Droplet motion induced by acoustic streaming.[92] (B) Three-dimensional droplet levitation in an acoustic potential trap.[112] (C) Droplet motion in a hydrodynamic trap generated by coupled bulk and surface acoustic waves.[105] (D) Droplet motion on an ultrasonically excited aluminum-alloy substrate.[93] (E) Directional motion of a Leidenfrost droplet on a ratchet surface.[113] (F) Self-rotation-driven mechanism for a Leidenfrost droplet on a ratchet surface.[114] (G) Leidenfrost droplet motion on a surface with a hydrophobicity gradient.[115]

imposed by the mode shape and the spatial position of the antinode.

Antinode-directed transport is not universal. Chen and Lal[118] used a horn-shaped silicon actuator operating in a half-wavelength longitudinal mode. They observed migration down the amplitude gradient toward a low-velocity node. In their interpretation, the droplet moves relative to the substrate only while the local velocity exceeds the contact-line threshold. Because the amplitude varies spatially, the positive and negative half-cycles generate unequal displacements and a net shift toward lower amplitude. Refs.[116,117] therefore describe an acoustic-radiation-dominated antinode regime, whereas Ref.[118] describes a node-directed regime governed by an amplitude gradient and a thresholded inertia–contact-line response.

Whole-substrate lateral, vertical, and multimode excitation uses the same mechanical input but different symmetry-breaking controls. Above an onset amplitude, asymmetric lateral vibration produces cycle-averaged inertial forcing on a droplet resting on a non-wetting surface.[119] Waveform asymmetry, contact-angle hysteresis, and nonlinear contact-line mobility make the forward and reverse half-cycles unequal, so their displacements do not cancel. Frequency, amplitude, waveform, and droplet resonance then set the speed and direction. Under vertical vibration, inclination supplies the spatial asymmetry. Above a critical acceleration, the cycle-averaged driving force can overcome the downslope gravitational component and move the droplet uphill.[120,121] This operating window depends on wettability; some more strongly hydrophilic liquids continued to move downhill as the vibration amplitude increased.[121]

Phase control provides another source of directional asymmetry. Noblin et al.[20] combined horizontal and vertical harmonic excitation at the same frequency and varied their relative amplitudes and phase difference. The horizontal component supplies periodic tangential forcing, while the vertical component modulates droplet deformation, normal load, and contact-line mobility. Symmetric horizontal excitation alone gives nearly cancelling half-cycle displacements. A phase-shifted vertical component makes the two contact-line responses unequal, breaks time-reversal symmetry, and produces net migration. Changing the phase therefore switches the droplet among forward motion, reverse motion, and a near-stationary state.

Substrate vibration supplies periodic mechanical energy, whereas vibration mode, waveform, phase, inclination, and contact-angle hysteresis determine whether that input is rectified into net motion. No responsive additive is generally required, but the migration direction, onset threshold, and transport efficiency depend on mode shape, frequency, amplitude, phase, droplet scale, liquid properties, and wetting state. Models that couple substrate dynamics, droplet resonance, contact-angle hysteresis, and viscous dissipation are therefore needed to construct dimensionless regime maps for direction, motion state, and onset.

Leidenfrost effect

Leidenfrost actuation converts heat supplied by a highly superheated substrate into vapor-mediated droplet motion while progressively consuming the droplet. The phenomenon was first described by Johann Gottlob Leidenfrost in 1756.[122] Vapor generated beneath the droplet forms a thermally insulating film that reduces direct solid–liquid contact, levitates the droplet, and slows further evaporation.[123] For a specified combination of liquid, heated-surface physicochemical and mechanical properties, and ambient conditions, the Leidenfrost temperature is the threshold at which a stable vapor film begins to exist and the lower boundary of film boiling.[124] This threshold, jointly set by the liquid, surface, and ambient environment, provides the operating-temperature baseline for the following discussion of vapor-film formation and ratchet transport. The substrate is the energy source, whereas the vapor film is the heat- and momentum-transfer medium. By reducing solid friction, the film facilitates motion.[94] When its pressure field or exhaust path is made asymmetric by surface texture, vapor pressure and shear can produce a horizontal force and select the trajectory.[94]

Ratchet textures impose directionality by making vapor discharge and droplet–surface coupling asymmetric. Linke et al.[113] observed motion down the inclined ratchet faces and attributed it to viscous shear from directed vapor flow beneath the droplet, as shown in Figure 5E. Dupeux et al.[125] traced vapor during dry-ice sublimation on a heated ratchet and found the vapor and dry-ice plate moving in the same direction, supporting this shear pathway. Because a rigid dry-ice plate lacks droplet deformation and internal circulation, however, that experiment does not determine which mechanism dominates for a deformable Leidenfrost droplet.

A second pathway becomes evident when internal circulation and droplet rotation are resolved. Mrinal et al.[114] observed simultaneous translation and self-rotation, while both the vapor flow and the motion at the droplet base were opposite to the translational direction. Viscous drag alone, thermal

creep,[126] and a rocket effect[127] could not account for this combination. The proposed sequence begins with a vertical temperature gradient that induces thermocapillary Marangoni circulation. The ratchet converts this circulation into droplet rotation, and asymmetric rotation–substrate coupling then produces translation, as illustrated in Figure 5F.

The dominant transfer pathway also changes with vapor-film state.[128] In the reported lower-temperature regime, an incomplete film allows local droplet–ratchet contact. Vigorous nucleate boiling then generates faster vapor flow, strengthens rotation, and increases translational speed. At higher surface temperature, a continuous film fully levitates the droplet and suppresses both direct contact and nucleate boiling. The associated vapor flow and rotation weaken, giving a lower translational speed in that regime.

Temperature can change not only the speed but also the direction of motion. On some ratchets, increasing temperature reverses translation because it changes the effective contact lengths on the vertical and inclined faces and hence the sign of the net horizontal force.[129] Leidenfrost propulsion must therefore be resolved by operating regime: vapor pressure, viscous shear, interfacial Marangoni flow, intermittent contact, and droplet rotation contribute with weights that vary with temperature and geometry. A regime map is more appropriate than assigning all observations to a single propulsion force.

Directional selection can also be imposed through a wettability gradient rather than a periodic ratchet. Femtosecond-laser processing created spatially differentiated micro/nanotopographies and a corresponding hydrophobicity gradient.[115] Under the reported conditions, the droplet migrated from the superhydrophobic region toward the less hydrophobic region, as shown in Figure 5G. The proposed mechanism is that the wettability contrast changes local vapor-film thickness, evaporation intensity, and flow resistance, thereby creating asymmetric pressure and velocity fields. Vapor then flows from the superhydrophobic side toward the less hydrophobic side and drives the droplet in the same direction through gas–liquid interfacial shear. Continuous control of laser-induced topography and wettability provides a fabrication route for nonperiodic high-temperature transport paths.

Leidenfrost systems separate the three functions that govern externally powered transport. Substrate heat supplies energy, vapor flow transmits pressure and shear, and texture or wettability asymmetry selects direction. Their engineering window is constrained by thermal demand, evaporation loss, limited controllability, and transitions among propulsion regimes. This division of function identifies an integration route between vapor-mediated forcing and the anisotropic rectifiers in Chapter 5. Its value must be assessed against droplet consumption and heat input.

ANISOTROPY OF LIQUID ACTUATION AND CONFINEMENT BY SOLID SURFACES

The preceding chapters classified how a driving force is generated by wettability gradients, curvature differences, or external inputs. This chapter addresses the complementary question of how asymmetric geometry and wetting boundaries select the transport direction. They create different capillary-advance conditions, interfacial resistance, and contact-line pinning barriers for opposing motions, so that liquid advances readily in one direction but encounters a larger barrier in the other. This liquid-diode behavior is a rectification function rather than an independent source of sustained energy. The required energy can still come from wetting free energy, gravity, droplet coalescence, vibration, or another external field. Rectification therefore complements the driving mechanisms described above.

Parallel grooves illustrate the distinction between directional guidance and rectification. A contact line moving across the grooves pins at their edges and exhibits greater contact-angle hysteresis or a higher critical sliding angle.[130] Motion along the grooves encounters less resistance. The hierarchical macro/micro/nanostructure of a rice leaf produces this transverse–longitudinal contrast. For the droplet volumes and inclinations tested, water preferentially rolled along the longitudinal grooves, while transverse barriers suppressed cross-groove motion.[131] Such guidance does not by itself distinguish forward from reverse motion along the same axis. Liquid-diode rectification additionally requires an asymmetric axial topology that gives the two directions different advance and pinning pathways. Repeating that unit can maintain directional selectivity, but the transport distance remains governed by liquid supply, gravity, external excitation, and interfacial dissipation.

Biological anisotropic structures

Biological surfaces combine hierarchical grooves, ratchets, microcavities, and interconnected capillary channels to regulate liquid-front pathways, capillary pressure, and contact-line pinning. Their functions should be compared by both energy source and rectification pathway. The cases below progress from passive capillary spreading and liquid-property-dependent selection to coalescence-powered motion and vibration-assisted detachment.

The pitcher-plant peristome[132] achieves passive capillary rectification by combining forward wedge imbibition with reverse edge pinning. Its superhydrophilic surface contains primary radial grooves, each with approximately ten secondary grooves. Partly overlapping duck-billed microcavities repeat along the secondary grooves. Each cavity has a closed top, sidewalls that narrow into a wedge, and a sharp terminal edge, as shown in Figure 6A. During outward spreading, capillary rise along the wedge displaces trapped air, fills the cavity, and promotes overflow into the next overlapping unit. In the reverse direction, the sharp edge and oppositely oriented wedge arrest the contact line. The same unit therefore provides low-barrier forward advance and high-barrier reverse motion, as illustrated in Figure 6B.[132]

The Concus–Finn criterion defines the wetting condition for capillary rise in a wedge.[133] For an ideal infinitely extended wedge, $\alpha+\theta<\pi/2$ yields no bounded equilibrium meniscus along the corner, where θ is the intrinsic contact angle and α is the wedge half-angle; equality is the critical boundary at which an equilibrium solution can exist. For a finite structure, the criterion specifies the wetting condition for corner imbibition and capillary rise, while the attained liquid height is set by the structural extent, liquid supply, and gravity. For a fixed narrow wedge satisfying the criterion, Chen et al.[132] used a local-equilibrium approximation for the liquid height H_e at transverse distance x from the apex:

$$H_e(x)=\frac{2\gamma_{lg}\cos\theta}{\rho a g x} \tag{22}$$

Here, γ_{lg} is the liquid–gas interfacial tension, ρ is the liquid density, and g is the gravitational acceleration. A wedge opening that decreases with height raises the local equilibrium level, and a closed cavity top can become completely filled.[133] The reverse boundary is set by Gibbs pinning at the sharp edge. For an ideal sharp edge on a chemically homogeneous surface under quasi-static conditions, the contact line remains pinned over the following apparent-contact-angle range:[134]

$$\theta_0\le\theta\le(180^\circ-\phi)+\theta_0 \tag{23}$$

Here, θ_0 is the intrinsic contact angle on the planar solid, θ is the apparent contact angle at the edge, and ϕ is the angle between the two faces forming the sharp edge; θ_0, θ, and ϕ are all expressed in degrees in this equation. The peristome integrates these capillary-advance and pinning conditions into one periodic rectifier. Wedge capillarity enables forward filling, while Gibbs pinning blocks reverse crossing.

Li et al.[139] transferred this asymmetric microcavity topology to a capillary inner wall. Compared with a smooth tube of the same scale, the structured tube increased both the rise rate and equilibrium height. In a candy-cane-shaped tube, forward capillary advance primed a continuous liquid column when the capillary rise reached the crest. An outlet below the reservoir level then supplied the hydrostatic head for sustained siphoning. Reversing the microcavities exposed overhanging edges to the advancing front, increased pinning, and impeded siphon initiation. The topology thus rectified the capillary-priming step rather than supplying the sustained siphon head.

Anisotropic structures can also use liquid properties to select among competing capillary pathways. Araucaria leaves[135] carry three-dimensional ratchets with transverse and longitudinal re-entrant curvature, as shown in Figure 6C. Spreading along the ratchet base and crossing its crest impose different capillary-advance and pinning barriers. Surface tension and apparent wettability change their relative magnitudes, so a liquid can spread with the ratchet tilt, against it, or in both directions, as illustrated in Figure 6D. Here,

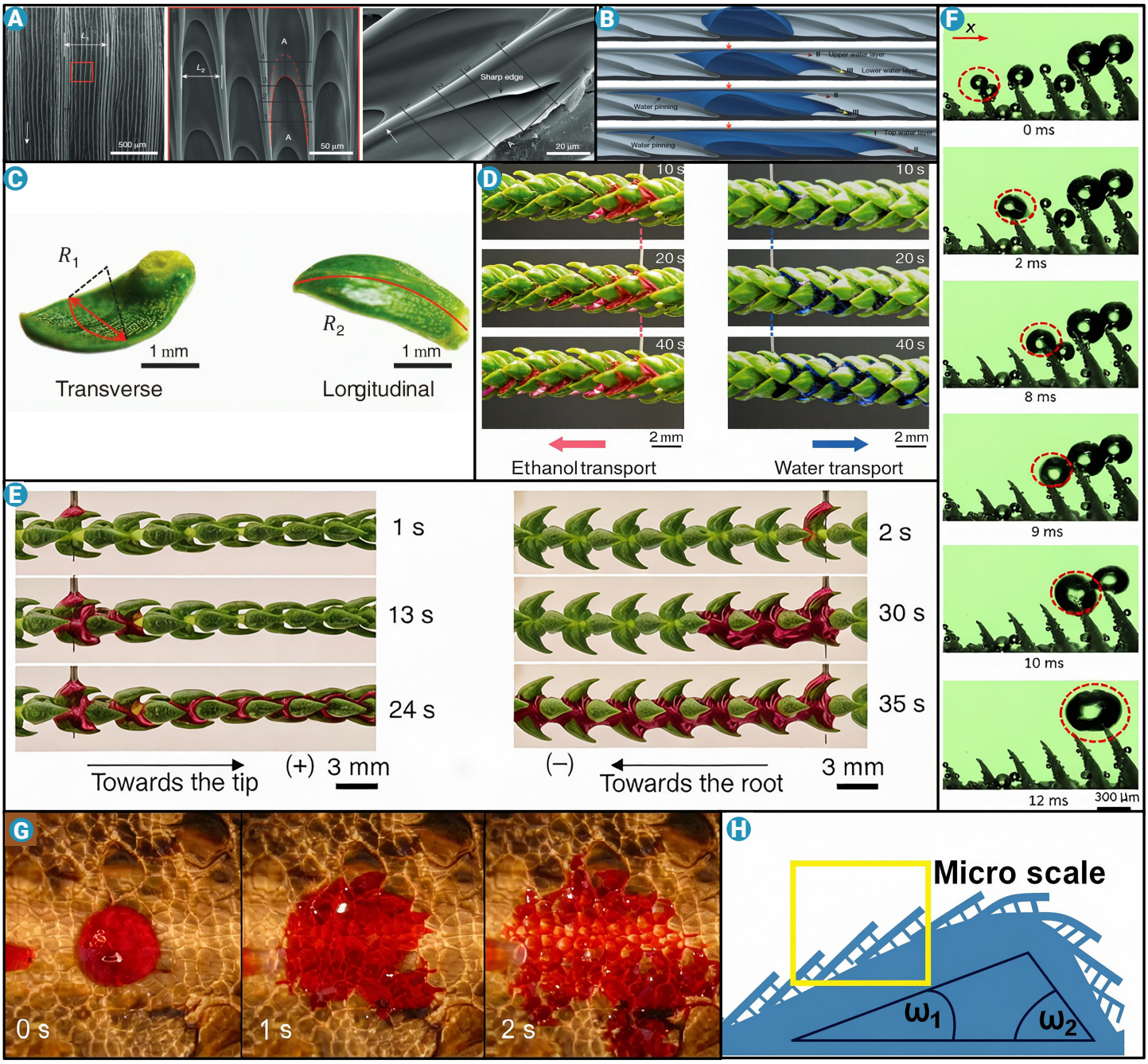


Figure 6. Biological anisotropic structures (A) Hierarchical grooves and microcavities on the pitcher-plant peristome.[132] (B) Unidirectional liquid spreading induced by the peristome structure.[132] (C) Structural characteristics of a single ratchet on an Araucaria leaf.[135] (D) Direction-dependent spreading of liquids with different surface tensions on an Araucaria leaf.[135] (E) Transport-direction control by leaf–stem angle combinations in Crassula muscosa.[36] (F) Directional coalesced-droplet motion on Chinese-juniper-inspired gradient Janus micropillars.[136] (G) Preferential water transport toward the mouth through the interscalar capillary network of the Texas horned lizard (Phrynosoma cornutum).[137] (H) Asymmetric ratchet structures on butterfly wings.[138]

interfacial free-energy reduction supplies the passive driving energy, while the ratchet maps liquid properties onto the preferred path.

In Crassula muscosa,[36] asymmetric concave leaves are staggered along the stem. The blade forms a forward angle ω_1, while the recessed base forms a backward angle ω_2. The combination of ω_1 and ω_2 sets the spreading mode. Liquid moves toward the tip, toward the base, or in both directions, as shown in Figure 6E. Corner capillarity at the leaf–stem junction helps the front cross a structural gap in the permitted direction, whereas geometric pinning raises the barrier in the opposite direction. A magnetoresponsive biomimetic analogue switches this rectification direction by changing the structural inclination under an external field.[36] The magnetic field reconfigures the boundary, while capillarity remains the direct driving mechanism.

Droplet coalescence provides an event-based energy source that can be rectified into in-plane motion. The scale-like leaves of Chinese juniper (Juniperus chinensis, reported as Sabina chinensis in Ref.[136]) combine inclined conical profiles, a height gradient, and Janus flat–curved tips. The corresponding gradient Janus micropillar array supports fog-droplet condensation, growth, and coalescence at the tips. Surface energy released by coalescence enables droplets to cross local barriers and launch toward increasing pillar height. Differences in contact area and adhesion between the flat and curved sides favor tip-induced flipping toward the curved side. Repetition of these asymmetric units converts local flipping into continuous directional transport, as shown in Figure 6F. Removing either the height gradient or the Janus geometry weakened directionality and continuity, separating the coalescence energy source from geometric rectification.[136]

The Texas horned lizard (Phrynosoma cornutum)[137] has superhydrophilic

honeycomb-like scale ornamentation and an interscalar capillary network that collects water and preferentially conducts it towards the mouth, as illustrated in Figure 6G. Frame-by-frame video analysis showed a higher rostral transport velocity than lateral and caudal velocities. Directional differences in channel cross section, branch connectivity, and the combination of dimples, protrusions, and folds can alter the local capillary pressure, viscous-flow resistance, and contact-line pinning encountered by the advancing front, providing a structural basis for preferential rostral transport. On Morpho deidamia wings, overlapping scales carry parallel ridges with inclined nanotips and form micro/nanoscale ratchets,[138] as shown in Figure 6H. Under static conditions, this asymmetry biases droplet growth, coalescence, and in-plane motion. Under vibration, it creates different pinning and detachment thresholds in opposing directions. The same topology therefore rectifies coalescence-related motion during static collection and externally supplied mechanical energy during vibrational removal.

Artificial anisotropic structures

Engineered surfaces need not reproduce the full hierarchy of a biological prototype. The transferable objective is to identify the geometric and wetting parameters that control advance and pinning, then reduce them to a repeatable rectifying unit compatible with fabrication tolerance and durability. The following examples illustrate four complementary design strategies: passive unidirectional rectification, multidirectional capillary guidance, vibration-powered rectification, and externally controlled directional switching. These strategies can be combined rather than treated as mutually exclusive categories.

Static topologies can sustain passive rectification when liquid is supplied continuously. Li et al.[12,140] placed U-shaped islands with re-entrant cavities inside periodic confining grids, as shown in Figure 7A. Interfacial free-energy reduction drove forward spreading, while the recessed-cavity edges suppressed reverse advance. Repetition of this unit maintained long-range unidirectional transport under continuous supply, as illustrated in Figure 7B. Within the reported temperature range, the topological rectification also exceeded the opposing thermocapillary tendency and preserved transport from the cold region toward the hot region. Building on geometrically prescribed transport, Sun et al.[141] combined macroscale tilted ratchets with re-entrant tips and oriented microgrooves. The microgroove layout adjusted spreading paths, while its orientation affected liquids with different surface tensions differently. This dependence indicates that path design must consider liquid properties alongside geometric orientation.

The coupling between liquid properties and surface geometry also appears in the curvature-ratchet study by Miao et al.[142] Varying structural parameters and surface-energy conditions enabled unidirectional, bidirectional, and reverse liquid manipulation. The authors defined $\zeta = \gamma_S/\gamma_L$, where γ_S is the solid surface free energy and γ_L is the liquid surface tension. Within the studied system, this ratio distinguished regimes with $\zeta > 1$, $\zeta \approx 1$, and $\zeta \ll 1$. Adjusting conditions near $\zeta \approx 1$ enabled modes including fan-shaped spreading, gradient-induced redirection, and reciprocating transport. The ratio therefore describes mode selection on these curvature ratchets, with applicability dependent on the specific geometry and wetting conditions.

Multidirectional routing is obtained by programming the orientation and connectivity of the rectifying units. Dai et al.[37] fabricated bulk–cusp arrays consisting of cross-shaped or square bulks and oriented cusps using photolithography and deep reactive-ion etching. Narrow gaps between adjacent cusps generate asymmetric capillary traction and guide a precursor film. The fraction of open area covered by that film determines whether it can pull the droplet body forward. Cusp orientation and array layout therefore select among pinning and one-, two-, three-, or four-directional spreading, as shown in Figure 7C. Sun et al.[143] instead used a fixed array of three-dimensional asymmetric fang-shaped units to obtain different preferred spreading directions for liquids with different surface tensions. Five modes were reported without rearranging the array, illustrating liquid-dependent directional selection on a fixed geometry, as shown in Figure 7D. Such selection differs from externally commanded, real-time switching of the transport direction for a given liquid.

Path selection can extend from the orientation of surface units to the connectivity of three-dimensional networks. Wu et al.[144] constructed a capillary-driven open fluidic network from polyhedral frames and connecting rods. The frames provide liquid storage and transport spaces, while rod number and arrangement control capillary connectivity between adjacent frames. Under the geometry and wetting conditions studied, spontaneous capillary flow required at least two rods, whereas a single-rod connection acted as a stop valve. Double-rod connections along target paths and single-rod connections elsewhere therefore confined flow to prescribed channels. Rod number, rod arrangement, and frame geometry also adjusted flow rate and distribution. This example extends prescribed-path guidance to three-dimensional networks, as illustrated in Figure 7E, although path selection alone does not establish rectification between forward and reverse transport.

Tilted nanostructures illustrate why the energy source must be separated from the rectifier. For the tilted-nanorod film in Ref.[145], random vibration supplies mechanical energy and the nanorod inclination converts it into droplet migration along the tilt direction, as shown in Figure 7F. Ref.[148] describes a distinct passive regime on discrete tilted nanopillars. There, wetting free energy drives spontaneous spreading, and unidirectionality appears only when the solid–liquid contact angle and pillar inclination satisfy the reported geometric–wetting condition. The two systems share structural anisotropy but not the same energy input.

Three-dimensional semicircular texture ratchets provide a second vibration-powered design.[27] Vertical excitation supplies energy, while unequal contact states at the leading and trailing edges make spreading, retraction, and detachment asymmetric and accumulate a net displacement over each cycle. Excessive vibration can trigger a Cassie–Baxter-to-Wenzel transition and immobilize the droplet, and the three-dimensional texture also complicates fabrication. Ref.[146] instead used a planar wetting barrier ratchet. Periodic semicircular hydrophilic domains on a hydrophobic substrate create direction-dependent contact-angle hysteresis and rectify orthogonal vibration, as shown in Figure 7G. Relative to the textured ratchet, this planar design requires a lower structural amplitude, simplifies fabrication, and can preserve optical transparency.

External control can reconfigure surface geometry to switch the transport direction on demand, extending the capabilities of fixed layouts. Son et al.[147] mounted superhydrophobic black-silicon strips on elastomeric ridges and added a soft-magnetic backing. Changing the magnetic-field position and strength tilted the strips in opposite directions and reversed the ratchet orientation. This geometric change established a switchable Laplace pressure gradient and enabled bidirectional droplet motion, as illustrated in Figure 7H. The magnetic field supplies the reconfiguration energy. The resulting Laplace pressure gradient provides the droplet-scale capillary force and selects its direction. Miao et al.[149] extended this approach using a hierarchical rectifier whose microratchet morphology was reshaped by a static magnetic field to regulate transport direction and mode. Under a uniform magnetic field, the microratchets bend collectively and uniformly, with the bending angle set by field strength and direction; this permits selective directional spreading of liquids with different surface tension. Under a non-uniform field, the microratchets adopt more complex three-dimensional morphologies and reconstruct microstructures unattainable under a uniform field, producing novel three-dimensional liquid-manipulation modes such as inchworm-like pulsatile liquid spreading.

External fields can also change wetting conditions and thereby regulate how a liquid interacts with an anisotropic structure. Miao et al.[150] used global and local temperature control on a PNIPAM-grafted heterostructured surface to achieve selective directional transport. Thermal regulation altered surface wettability and consequently modified the conditions for structure-mediated directional selection. Under the reported conditions, local temperature control could compete or cooperate with structural effects and reverse the transport direction. Here, the relevant contribution is the modulation of structural guidance by thermoresponsive wettability. Direct thermally induced driving forces should be distinguished using the mechanisms discussed in Section 2.

Repeated asymmetric units can extend directional selectivity beyond a single macroscopic gradient, but they do not remove the energy and supply constraints on transport. An anisotropic surface establishes the boundary conditions and energy landscape that rectify interfacial free-energy reduction, gravitational potential energy, coalescence, impact, vibration, or another external-field input. Continuous spreading requires an adequate reservoir or

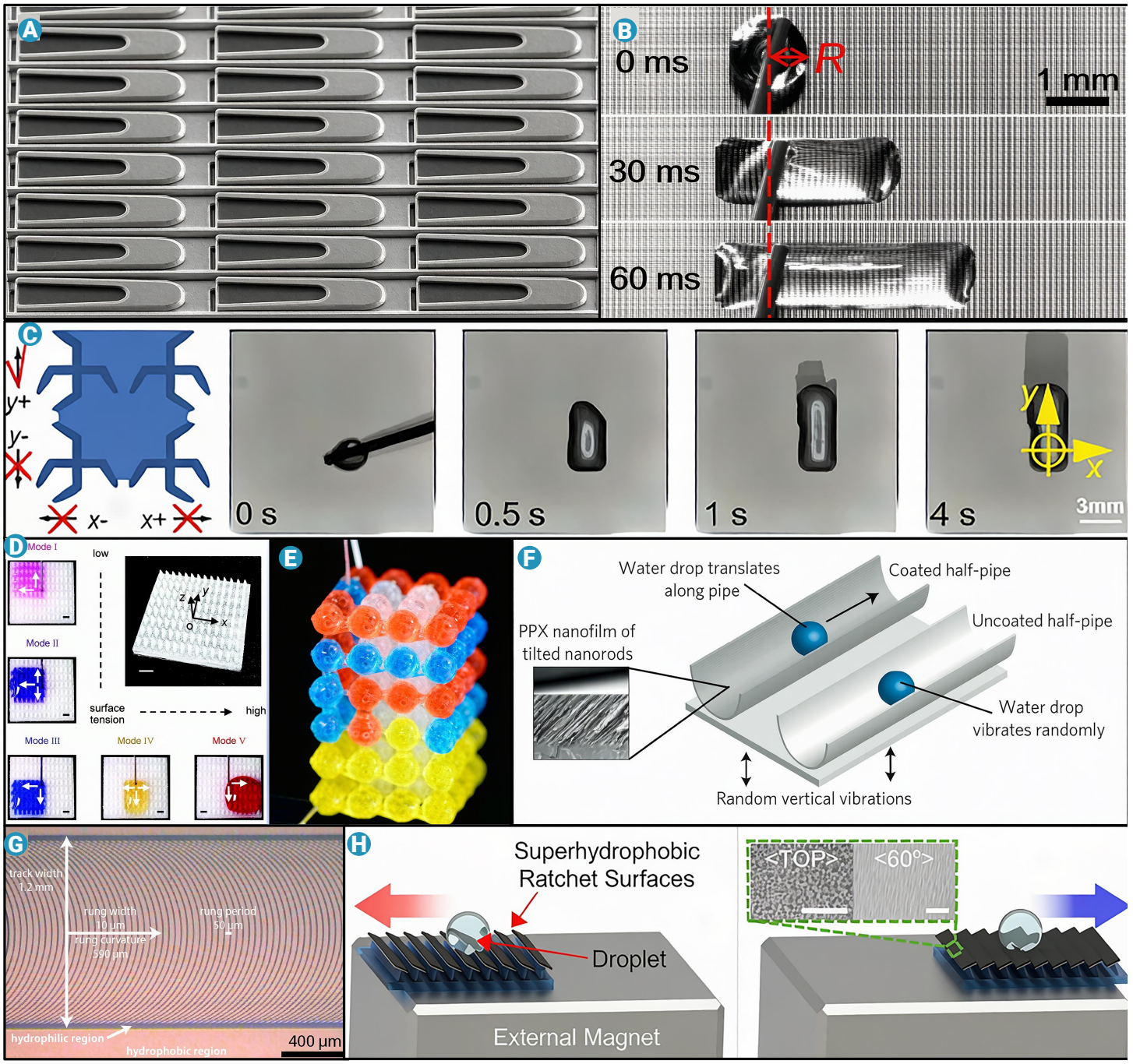


Figure 7. Artificial anisotropic structures (A) Asymmetric surface comprising U-shaped islands and re-entrant cavities.[12] (B) Unidirectional liquid spreading on a U-shaped cavity array.[12] (C) Multidirectional spreading regulated by bulk–cusp microstructures.[37] (D) Five spreading modes of liquids with differing surface tension.[143] (E) Programmable spatiotemporal control of multiple continuous flows in three-dimensional space.[144] (F) Vibration-driven droplet migration on a tilted-nanorod film.[145] (G) Planar wetting barrier ratchet with periodic semicircular hydrophilic patterns on a hydrophobic substrate.[146] (H) Directional droplet motion on a magnetically reconfigurable ratchet array.[147]

sustained liquid supply. Sustained or repeated transport of discrete droplets also requires available energy appropriate to the system. Sources may include wetting free energy, impact, coalescence, or continuous external excitation. Engineering translation is further limited by reliance on biomimetic replication, trial-and-error optimization, and geometry-specific correlations, which restrict predictive transfer among designs. Complex topologies also remain difficult to manufacture with low cost, short cycle time, and high yield. Mechanism maps, minimum functional units, and fabrication-aware models provide the design basis for scale-up.

CROSS-MECHANISM COMPARISON AND DESIGN IMPLICATIONS

Figure 8 compiles 29 velocity–distance records from 23 studies, each pairing the same transported object either within a single motion event or under matched nominal conditions. The liquid, transported volume, substrate inclination, energy input and run mode behind each record are listed in Supplementary Table 2. The left panel, referred to as (A), contains 26 discrete-droplet records from 21 studies, whereas the right panel, referred to as (B), contains three records of continuous-liquid, liquid-finger, meniscus or wetting-front advance from three studies. Colour distinguishes surface/interfacial-tension asymmetry, curvature-induced Laplace pressure gradients, external forcing and anisotropic rectification on solid surfaces. Circles, triangles and diamonds denote pre-patterned/passive surfaces, runtime-programmed actuation and event/periodic rectification, respectively. Filled markers indicate values reported directly or derived from same-condition time–displacement data, open markers denote figure-derived records, and † identifies net displacement per cycle and its cycle-equivalent velocity. Identical logarith-

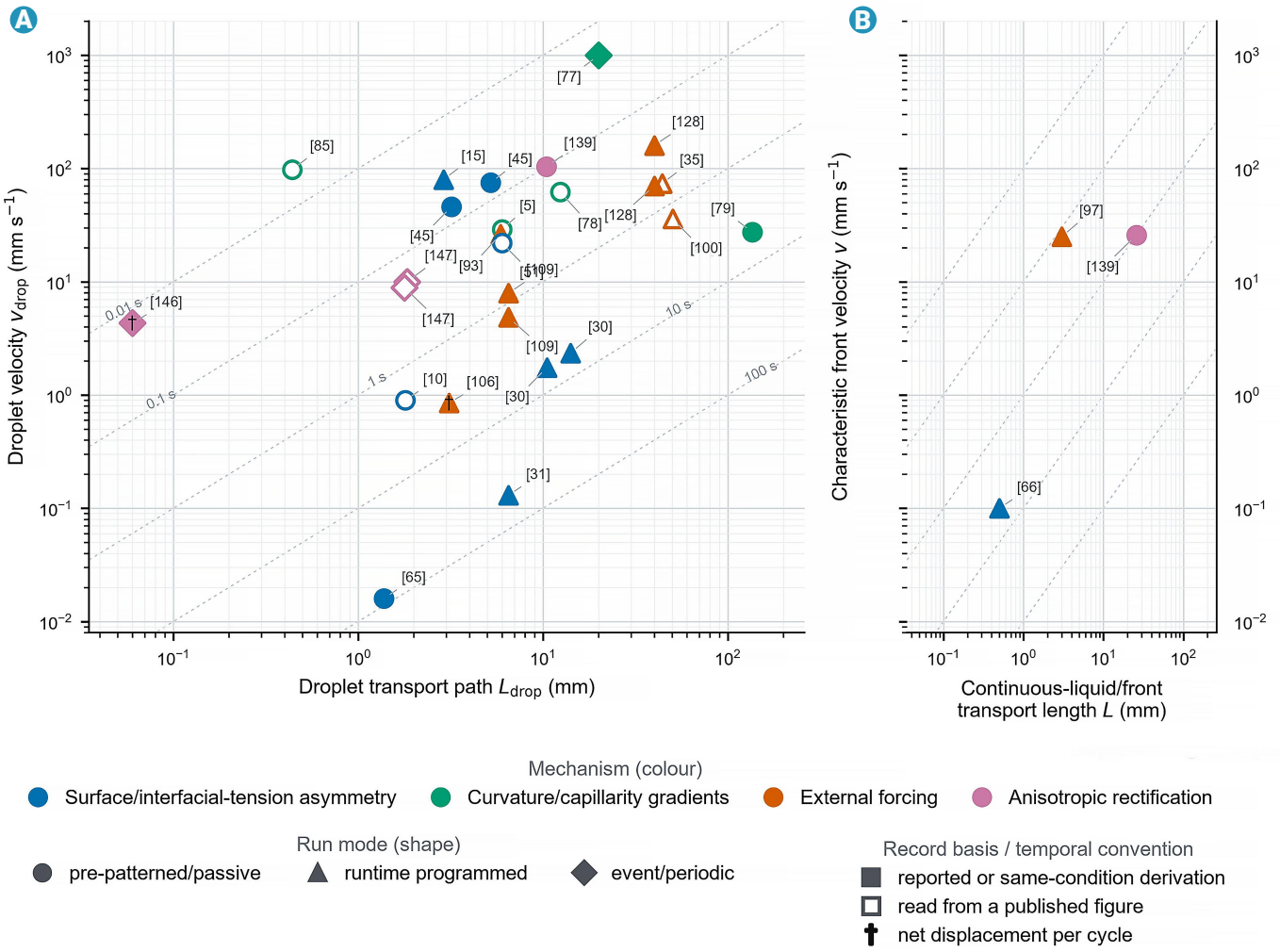


Figure 8. Velocity–distance operating windows for directional liquid transport on solid surfaces: discrete droplets and continuous liquids/fronts The left panel (A) shows discrete-droplet migration. The axes report the transport path L_{drop} and corresponding velocity v_{drop} of an identifiable droplet within the same motion event or under matched nominal conditions, comprising 26 records from 21 studies. The right panel (B) shows continuous-liquid/front advance. The axes report the distance L and characteristic velocity v of a continuous liquid, liquid finger, meniscus or wetting front within the same observation window, comprising three records from three studies. Both panels use identical logarithmic limits; grey dashed lines denote $t = L/v$ for kinematic order-of-magnitude comparison. Colour denotes the mechanism class; circles, triangles and diamonds represent pre-patterned/passive surfaces, runtime-programmed actuation and event/periodic rectification, respectively. Filled and open markers distinguish direct or same-condition values from figure-derived values, and † denotes net displacement per cycle with the corresponding cycle-equivalent velocity. The right panel characterizes continuous-liquid motion using transient front velocity and advance distance. The number of each data ponits refer to its referece number. Ref.[139] contributes one discrete-droplet record and one continuous-front record. The point from Ref.[77] is plotted using a source-reported characteristic estimate for a biological capillary ratchet.

mic axes and $t = L/v$ lines allow kinematic comparison of fast but short-range, slow but long-range, and fast and long-range windows. Velocity in the left panel (A) describes translation of an identifiable droplet, whereas velocity in the right panel (B) describes advance of a front or meniscus connected to a liquid reservoir. The v–L–t coordinates therefore provide a common kinematic scale, while throughput, pressure head and energy efficiency are evaluated according to the transported object and its boundary conditions. The operating windows can be reduced to three design variables: energy supply determines sustainable driving, interfacial and geometric design determine resistance reduction, and structural asymmetry determines rectification and directional selection. With transport objects and boundary conditions defined, the map supports mechanism selection and task matching.

Mechanism comparison and operating windows

Surface/interfacial-tension asymmetry comprises nine records in Figure 8A, spanning 0.016–80 mms^{-1} over paths of 1.38–14.1 mm, from millimetric to centimetric distances. The common starting point is a difference in wetting state or interfacial tension between the front and rear contact lines. The decrease in interfacial free energy along the direction of motion produces a net force dominated by a Young-force imbalance; thermoresponsive systems may additionally introduce a co-directed Marangoni stress. The broad velocity distribution is governed by how this driving is constructed and matched to contact-angle hysteresis, viscous dissipation and adverse gravity. The rapid, short-path boundary is defined by Ref.[45] & [15], where droplets reach 46–80 mms^{-1} over 2.9–5.2 mm. Together, these records show that a strong wettability contrast is converted efficiently into whole-body translation only when paired with a low-hysteresis interface. Intermediate records reveal two ways to sustain driving. Radial trapezoidal microgrooves in Ref.[51] couple wettability and capillary-pressure gradients while promoting a Wenzel-to-Cassie transition that reduces hysteresis, moving a droplet over 6.0 mm at a figure-derived velocity of approximately 22 mms^{-1}. In Ref.[30], a persistent photothermal wetting response extends the path to 10.5–14.1 mm, while the velocities of viscous liquids decrease to 1.75–2.35 mms^{-1}. This comparison shows that path length depends on whether the interfacial-free-energy gradient persists along the route, whereas velocity is jointly controlled by interfacial-state transitions and viscous dissipation. The low-velocity boundary further identifies operation near the resistance threshold. The inclined wettability gradient in Ref.[10] still drives a droplet at approximately 0.9 mms^{-1} against adverse gravity and hysteresis, whereas the weak molecular-machine-induced surface-energy gradient in Ref.[65] yields 0.016 mms^{-1} over 1.38 mm. The design task is therefore to preserve a co-directed decrease in interfacial free energy along the path while retaining a sufficient forward driv-

Table 2. Application-specific transport modes, mechanisms, performance metrics, and practical limitations of directional liquid transport on solid surfaces

Application	Main transport modes	Driving pathways and directional-control functions	Key performance metrics	Practical limitations
Phase-change heat transfer	Directional liquid replenishment of heated surfaces through anisotropic channels or capillary wicks; directional shedding and sweeping of condensate droplets; capillary liquid return from the condenser to the evaporator	Capillary action in anisotropic grooves or porous wicks; Laplace pressure differences arising from curvature differences; wettability gradients; local field-assisted regulation	Boiling/evaporation: heat-transfer coefficient, critical heat flux (CHF, for boiling conditions), and time to dryout under a specified thermal load (for transient tests); dropwise condensation: heat-transfer coefficient, critical droplet-shedding diameter, and sweeping frequency; devices with capillary return: maximum heat-transfer rate at the capillary limit and pressure drop at a specified liquid return rate	Vapour blockage of liquid supply channels; condensate accumulation or flooding of microstructures; additional condensation mass-transfer resistance from non-condensable gases; changes in wettability caused by high-temperature oxidation, scaling, or coating ageing; wick clogging; large-area fabrication uniformity and cost
Fog harvesting	Capture, coalescence, and directional transport of discrete droplets, followed by quasi-continuous drainage	Curvature differences generated by wedge-shaped or conical structures; wettability gradients; guidance and rectification of capillary motion by bioinspired anisotropic structures	Water collection rate per unit area; fog-droplet capture efficiency; droplet transport or shedding time; fraction of water lost to evaporation; long-term retention of collection rate	Dependence on wind speed, fog liquid water content, and droplet size distribution; surface contamination and salt deposition; drainage obstruction by frost or ice; array shielding and drainage interference that constrain scale-up; weathering resistance and long-term chemical stability
Microfluidics	Programmable addressing and routing of discrete droplets; directional transport and branch selection of continuous liquid streams or advancing fronts	Electrowetting, dielectrophoresis, thermal or photothermal Marangoni stresses, and magnetic or acoustic actuation; capillary pressure differences and structural guidance; auxiliary rectification by anisotropic structures	Command execution success rate; positioning accuracy (including single-step displacement error); minimum controllable droplet volume; response time and parallel processing throughput; flow-rate stability and branch allocation accuracy for continuous flows; cross-contamination level	Dielectric-layer ageing and breakdown in electrowetting-on-dielectric devices; effects of liquid conductivity, surface tension, and wetting state on actuation; surface adsorption and residual liquid; integration complexity of actuation, sensing, and control systems; throughput constraints imposed by addressing speed, interference between parallel operations, or flow coupling between branches

Table note: The listed mechanisms and limitations are representative and depend on device configuration and operating conditions. Comparisons should specify relevant liquid properties, supply conditions, orientation relative to gravity, and external inputs, together with thermal loads for heat transfer and incident fog conditions and collection-area definitions for fog harvesting.

ing margin through low contact-angle hysteresis and controlled viscous dissipation.

Unlike surface/interfacial-tension asymmetry, which is dominated by a Young-force imbalance between the contact lines, curvature-induced transport is driven directly by a Laplace pressure difference created by unequal front and rear meniscus curvatures. The five records in Figure 8A span 27.4–1000 mms^{-1} and 0.44–136 mm and can be interpreted through a sequence of pressure generation, dissipation suppression and pressure renewal along the route. The upper velocity bound comes from the source-reported estimate in Ref.[77], based on a characteristic transport length of about 2 cm and a characteristic time of about 20 ms in a shorebird bill. Periodic opening and closing reshape the curvature field in the wedge, while contact-line pinning rectifies the reciprocal geometric input into net motion towards the mouth. The estimate of approximately 1000 mms^{-1} characterizes the response of biological dynamic-curvature reconfiguration; the rapid, short-path boundary for engineered surfaces is defined by Ref.[85], in which a nascent droplet on a liquid film travels 0.44 mm at a figure-derived mean velocity of approximately 98 mms^{-1}. Film lubrication suppresses contact-line dissipation and rapidly converts a local curvature contrast into translation, but the path remains limited by the nascent-droplet scale and local film extent. Records Ref.[5] & 78 demonstrate two intermediate-distance strategies. In Ref.[5], coupled structural and wettability gradients move a 3 μL droplet over approximately 6.0 mm at 29 mms^{-1}. Control experiments identify the aligned chemical wettability gradient as the element that increases net driving and lowers subsequent contact-angle hysteresis, extending local curvature/structural driving to intermediate distances. In Ref.[78], a 20 μL water droplet travels 12.4 mm at 62 mms^{-1} in a humidity-responsive open conical channel. Humidity-induced switching reconfigures the two-wire geometry and establishes a Laplace pressure difference in the open conical state, while a low-hysteresis superhydrophilic interface converts that pressure difference into effective transport. Long-range transport further requires pressure renewal: in Ref.[79], a 0.8 mL droplet crosses seven wedge nodes over 136 mm at a source-reported full-path mean velocity of approximately 27.4 mms^{-1}, although each node also introduces reverse Laplace contributions, wall resistance and centre-of-mass lifting. The design task is therefore not simply to maximize the initial curvature contrast, but to suppress contact-line or film dissipation while constructing a renewable capillary-pressure network in which the forward capillary force remains greater than the capillary resistance associated with contact-angle hysteresis, viscous wall resistance and adverse gravity throughout the route.

External forcing changes the temporal character of driving. Unlike passive systems that depend on pre-patterned gradients or fixed geometry, optical, thermal, acoustic, magnetic and vapour-mediated fields can be sustained, translated or reconfigured while a droplet moves. The eight records in Figure 8A span 0.85–160 mms^{-1} and 3.1–50.3 mm, with the velocity–distance window governed first by how the net driving is maintained in space. Records Ref.[100], [35] & [128] sustain driving during advance by translating the direction of dielectric forcing, moving an energy minimum, or coupling vapour flow to ratchet geometry, respectively. They consequently maintain 35.9–160 mms^{-1} over 40–50.3 mm and jointly define the fast-and-long window. A fixed acoustic field provides the complementary mode by writing the driving landscape around a prescribed destination. In Ref.[93], a droplet travels 5.9 mm at 26.3 mms^{-1} towards a standing-wave antinode and stops as the acoustic actions at its front and rear approach balance. The two field modes therefore separate functionally: moving or distributed fields extend the path by preserving a non-zero force gradient, whereas a fixed potential well uses terminal

force balance for target capture without real-time tracking. Spatial persistence sets the reachable path, while actual velocity is further modulated by energy-conversion efficiency and effective actuation time. The higher velocity at 250°C than at 350°C in Ref.[128] shows that thermal input must be converted through the vapour-layer state into interfacial driving, so stronger input does not necessarily produce stronger effective driving. The cycle- or step-averaged velocities of 0.85–7.94 mms^{-1} in Ref.[106] & [109] further show how non-propulsive intervals associated with capture, adhesion, acceleration, deceleration and release reduce the process-averaged transport rate. The operating boundary of external forcing can thus be organized around three connected controls: spatial persistence of the force gradient sets path length, conversion from input energy to interfacial driving sets the instantaneous response, and actuation duty sets the process-averaged velocity. Together they enable remote, reversible and programmable control while defining the engineering balance among field-source power, execution time and device integration.

Anisotropic rectification plays a role distinct from that of the preceding three mechanisms. Rather than establishing an independent, sustained primary driving force, it imposes directionality on available energy inputs through asymmetric textures, oriented structures and contrasts between advancing and receding contact-line thresholds. Its four records in Figure 8A span 4.32–104.2 mms^{-1} and 0.060–10.42 mm, a range that primarily reflects differences in the energy-supply event and interfacial state. A planar wetting-barrier ratchet in Ref.[146] produces 0.060 mm net displacement per cycle under 72 Hz vertical vibration, equivalent to 4.32 mms^{-1}: vibrational input first overcomes unequal depinning barriers at the two edges, and net directional displacement arises only during cycle phases in which one side depins while reverse motion remains pinned. In Ref.[139], a subsequent water droplet on a prewetted peristome surface travels 10.42 mm in 0.10 s at 104.2 mms^{-1}. The prewetted, low-resistance interface reduces contact-line dissipation and establishes a continuous capillary pathway, converting the directional selectivity of microgrooves into rapid transport. In Ref.[147], magnetic reversal of superhydrophobic-ratchet polarity directs impacting droplets leftward and rightward over 1.78–1.84 mm at 8.9–10.0 mms^{-1}; the field switches structural orientation, whereas local imbibition and curvature response determine the ensuing motion. Anisotropic structures are therefore best assigned the roles of droplet diode, splitter or router, coupled with modules that provide capillary, interfacial, impact or external-field energy to select direction, suppress reverse motion and allocate paths.

Figure 8B reveals two operating modes for continuous liquids. Electrowetting resets the contact angle and capillary equilibrium position, producing slow, reversible interface switching at approximately 0.1 mms^{-1} over 0.5 mm.[66] DEP fingers and oriented capillary structures instead occupy a rapid-front window near 25 mms^{-1}.[97,139] The latter two attain similar mean velocities, but their advance boundaries are controlled by different conditions. The finite electrode region defines the approximately 3 mm finger-advance distance in Ref.[97]. Within this local field, the non-uniform electric field draws a finger from the mother droplet, and the dynamics ultimately approach a balance between DEP driving and capillary restoration. By contrast, the precursor film in Ref.[139] forms confined hydrophilic walls with a near-zero contact angle, maintaining a concave moving meniscus and a forward capillary pressure. With reservoir supply, bulk water achieves a same-window net rise of $\Delta H \approx 25.83$mm over 0–1 s while accumulating viscous loss and hydrostatic head as the filled length grows. The approximately 8.6-fold path difference is therefore consistent with two boundary conditions: a local finger within a finite electrode region and reservoir-fed capillary rise. The actual advance distance is jointly set by the driving region, geometric length, reservoir condition and terminal balance. Their mean velocities near 25 mms^{-1} indicate only similar kinematic responses over the selected time windows; front velocity itself results from the combined effects of net pressure, cross-section, hydraulic resistance, inertia and observation window. This comparison also clarifies the design distinction between the two panels. A discrete droplet remains approximately fixed in volume, and its velocity–distance window reflects the net margin by which whole-body translational driving overcomes contact-line hysteresis and viscous dissipation. A continuous front progressively wets new wall area and mobilizes an increasing liquid inventory, so its pressure budget must additionally cover the viscous loss accumulated with filled length and, where applicable, hydrostatic head. Droplet design therefore emphasizes sustaining the net driving for whole-body translation, whereas continuous-liquid design jointly matches front velocity, flow rate Q, capillary head and supply stability.

Strengths and limitations of driving pathways and directional control. Pre-patterned wettability gradients can drive transport without continuous external power, whereas thermally, optically, or electrically regulated interfaces can enable dynamic control of transport, with path reconfiguration possible in suitable designs. Their operating range depends on the available interfacial free energy, gradient extent, contact-line hysteresis, and surface stability; electrowetting additionally faces contact-angle saturation and dielectric breakdown. Curvature-induced Laplace pressure differences can be established without a spatial chemical pattern, but fixed geometries constrain the accessible route, and viscous losses and hydrostatic head limit the distance and flux attainable under a given supply condition. Successive curvature units can establish local pressure differences as the liquid front advances, while reconfigurable geometries can modify these differences during operation. External-force actuation provides adjustable forcing and, in suitable implementations, reversible, programmable, remote, or noncontact control, at the cost of power delivery, control hardware, and integration. Acoustic and vibrational routes depend on excitation modes and calibration, while Leidenfrost transport requires elevated substrate temperatures and is accompanied by evaporation. Anisotropic boundaries can guide spreading, suppress backflow, or support splitting and routing, depending on their geometry and wetting conditions. Structural anisotropy alone, however, does not provide a sustained energy supply. The effectiveness of these directional-control functions depends on a driving input, liquid supply, and the stability and manufacturability of the boundaries. Application matching therefore requires joint evaluation of the driving pathway, liquid-supply arrangement, and directional-control function against the required flow rate or droplet-handling performance and operating conditions.

Design implications and task-oriented architectures

From velocity–distance windows to design principles. Figure 8A shows that surface/interfacial-tension-asymmetry systems generally remain within 14.1 mm. Their pre-patterned wettability gradients release finite interfacial free energy through a Young-force imbalance between the front and rear contact lines and are therefore suited to initiation and short-range propulsion. Curvature/capillary transport extends both velocity and distance limits. Periodic opening and closing of an avian bill dynamically reconfigure the curvature field and raise the characteristic velocity to approximately 1000 mms^{-1},[77] whereas serial curvature units establish and renew Δp_L through differences in meniscus curvature and extend the path to 136 mm.[79] The former shortens the capillary response time, while the latter extends the distance over which a forward pressure difference is sustained; together, they show that curvature design can strengthen transient driving or enable long-range transport through pressure renewal. Sustained fields or translated potential wells maintain 35.9–160 mms^{-1} over 40–50.3 mm,[35,100,128] demonstrating how runtime energy supply supports the fast-and-long window. These windows can be organized by how driving is maintained in space and time: interfacial free energy is released along a pre-patterned gradient, capillary pressure is renewed geometrically along the route, or field energy is supplied continuously during operation. A second design layer is set by how the transported object evolves. An approximately fixed-volume droplet mainly encounters contact-line hysteresis and whole-body translational dissipation. A reservoir-fed continuous front also increases liquid inventory and wetted length, so matching energy supply to resistance reduction must cover the viscous pressure loss accumulated along the path and, where applicable, hydrostatic head. Task architecture therefore requires two mappings: the transported object and boundary conditions determine how resistance evolves, while the pre-patterned gradient, geometric pressure renewal or runtime field determines the spatial scale of driving. On this basis, cross-mechanism cooperation is not a simple superposition of driving modes. Instead, it assigns energy supply, resistance reduction and rectification to units with matched physical roles, so that the generated driving retains a sufficient forward pressure margin along the full path. Effective gain first arises from improving transmission of that driving: low-hysteresis interfaces reduce the contact-angle-

hysteresis threshold Δp_{CAH}; a controlled thin liquid film replaces part of the solid–liquid contact with a liquid–liquid shear interface and alleviates contact-line dissipation; gradual nodes renew local Δp_L while reducing the additional cross-node loss Δp_{node}; and anisotropic boundaries separate advancing and receding thresholds to release the retained pressure margin selectively along the target direction. Conversely, roughness or chemical discontinuities without a low-hysteresis design raise Δp_{CAH}; excessively thick or unstable films both alter meniscus shape and increase the distributed viscous pressure loss Δp_μ; and steep or discontinuous curvature nodes introduce reverse Laplace pressure and localized wall dissipation. Curvature–wettability cooperation therefore does not seek to maximize Δp_L or the pressure-equivalent wettability contribution Δp_W in isolation. It aligns the two and maintains their combined gain above distributed and cross-node losses. For such passive architectures, the local pressure-balance criterion is

$$\Delta p_L + \Delta p_W > \Delta p_{CAH} + \Delta p_\mu + \Delta p_{grav} + \Delta p_{node} \quad (24)$$

where Δp_L and Δp_W are the effective contributions from curvature and aligned wettability bias, respectively. Δp_{CAH}, Δp_μ and Δp_{grav} are the equivalent pressure losses caused by contact-angle hysteresis, distributed viscous dissipation and adverse gravity. Δp_{node} is the additional pressure loss across a node, including reverse Laplace pressure and localized viscous wall losses; local pinning appears as a local increase in Δp_{CAH}.

Task–architecture map. For discrete droplets, pre-patterned wettability gradients suit short-range, low-cost passive transport;[45] cascaded curvature structures suit long-range passive transport with staged velocity adjustment;[79] and a cascaded-curvature backbone with a low-hysteresis aligned wettability bias addresses passive, long-range and rapid return. Optical, thermal, acoustic or magnetic fields enable rapid, reversible and complex-path manipulation,[35,93,100,106,109,128] whereas anisotropic rectification modules provide backflow suppression, one-way selection and splitting.[139,146,147] For continuous liquids, electrowetting menisci provide reversible interface switching,[66] transient DEP fingers provide short-range on-demand liquid distribution,[97] and oriented capillary structures provide passive replenishment or anti-gravity front advance.[139] Performance evaluation for continuous transport therefore extends from velocity and distance to flow rate, pressure head, channel cross-section, reservoir boundary condition, gravity orientation and long-duration stability. This map turns the static question of which mechanism is faster into a design question of what is being transported and which driving source, loss-control strategy and direction-management method best match the task.

Application-specific performance criteria. Transport velocity and distance characterize how fast and how far liquid moves, but do not by themselves establish whether an application meets its performance requirements. Table 2 links representative applications with transport modes, driving pathways, directional-control functions, performance metrics, and practical constraints. Comparisons should therefore be made within a defined application under matched operating conditions.

Illustrative design concept: curvature–wettability cooperation for passive liquid return. The preceding principle requires energy supply, resistance reduction and rectification to be distributed in sequence along the route, rather than simply superimposing surface features in the same region. One implementation is a bamboo-node cascaded-wedge channel with a graded wettability bias: a low-hysteresis receiving zone is followed by repeated outer-wedge driving, inner-wedge transition and bamboo-node segments, which terminate in an expanded collection cavity. The transport backbone adopts the outer-wedge/inner-wedge/vertical-wall combination.[79] The outer wedge creates a difference between the front and rear meniscus curvatures in the driving segment, while the inner wedge remains in contact during node crossing and provides auxiliary capillary traction, thereby renewing the local Laplace pressure difference from one segment to the next. A pre-patterned wettability bias need not be restricted to a gradient in the area fractions of superhydrophobic nanopillars and hydrophilic SiO_2 stripes.[45] It can also use a fixed surface-chemical functional-group coverage gradient,[13] or trapezoidal microgrooves and ridges beneath a uniform low-surface-energy coating, where the structure itself generates coupled wettability and capillary-pressure biases.[51] In the proposed architecture, each implementation is placed on the floor or sidewalls of the outer-wedge driving segment and provides a weak, continuous wettability bias aligned with the transport direction. It lowers the initiation threshold, compensates local pressure decay after a node and suppresses backward motion, rather than supplying the primary driving over the full route. At the inner-wedge/vertical-wall transition, shallow microgrooves parallel to the transport direction can follow the axial-gradient microchannel concept of conical setae in Ref.[85]. Condensate then maintains a thin liquid film only near the node, where a liquid–liquid shear interface reduces cross-node contact-line dissipation. A more wettable inlet to the expanded terminal cavity receives the droplet. In this layout, reduction of the total interfacial free energy of the droplet–solid–gas system supplies the passive transport energy; outer-wedge and node geometry establish and renew the Laplace pressure difference in stages; the pre-patterned wettability bias supplies a co-directed Δp_W and lowers the initiation threshold; the local thin film reduces cross-node contact-line dissipation; and the bamboo-like nodes together with the wettability-bias direction provide one-way rectification. These control variables can be optimized jointly around the local pressure-balance criterion defined above. If the architecture is extended from discrete-droplet return to a continuous return channel, the optimization target shifts from the droplet velocity–distance window to a multi-objective balance among flow rate, pressure head and stability, with cross-sectional area, distributed pressure loss and reservoir boundary conditions included as constraints.

CONCLUSIONS AND PROSPECTS

This review organizes directional liquid transport using two linked questions: where does the droplet-scale driving force originate, and what selects its direction? Surface/interfacial-tension asymmetry, curvature-induced Laplace pressure gradients, and external-force actuation answer the first question. Anisotropic solid surfaces answer the second by imposing asymmetric capillary advance, contact-line pinning, and interfacial resistance.

Based on the above comparisons and the mechanistic framework outlined earlier, this conceptual separation of force generation from directional rectification leads to three conclusions for mechanism selection, coupled design, and engineering translation.

(1) Different driving mechanisms have distinct operating conditions and performance boundaries. Spatial gradients in chemical composition, surface roughness and geometric curvature can enable spontaneous transport through changes in interfacial free energy and generally do not require sustained external energy input; however, the free-energy decrease available to a droplet and the spatial extent of the gradient together limit its transport distance and controllability. Electric, magnetic and acoustic fields, substrate vibration, and vapour layers induced by heated substrates can provide sustained or programmable energy input, offering advantages in response rate, transport direction and path control, but their performance depends on liquid properties, material response, field strength and device integration. Anisotropic surfaces can produce liquid-diode-like rectification through periodic asymmetric units, reducing reliance on continuous macroscopic gradients, although the structures themselves are generally not independent energy sources. Long-range transport of continuous liquids also requires sufficient liquid inventory or sustained supply, whereas the migration of discrete droplets may draw energy from deposition, gravitational potential release, coalescence or mechanical vibration. Future studies should therefore identify minimum structural units responsible for energy supply, resistance reduction and rectification, and report droplet volume, surface state, velocity, path, onset threshold, cycling stability and energy consumption under comparable conditions, so that mechanisms can be compared by operating windows rather than isolated peak values.

(2) Multimechanism systems should be co-designed by assigning distinct roles to energy supply, force transmission, directional selection, and dissipation, then matching their magnitudes and timescales. On PNIPAAm-grafted surfaces, a temperature gradient generates thermowetting and Marangoni-stress contributions that act in the same direction. Spider silk and cactus spines coordinate conical geometry, grooves, and wetting characteristics across capture, coalescence, and transport. Chinese-juniper-inspired Janus micropillars use coalescence as the energy source and geometric asymmetry to select how that energy is released. Vibration-coupled ratchets make the

same division explicit: vibration supplies mechanical energy and the anisotropic boundary rectifies it. Coupled design should therefore place all driving and resisting contributions in a consistent force or energy balance, identify reinforcement or cancellation, and optimize the combination for the intended onset threshold, speed, flux, or switching function.

(3) Shifting from imitation of biological structures to mechanism extraction and rational design is essential for improving structural predictability and engineering manufacturability. Biological surfaces commonly exhibit multi-scale features, including hierarchical grooves, tapered profiles, microcavities and ratchets, whose transport functions generally arise from the coupling of capillarity, curvature differences, wettability contrasts and contact-line pinning rather than from an isolated geometric feature. Faithfully reproducing such complex morphologies is not necessarily required to achieve high-performance transport. Future studies should further identify the minimum structural units responsible for energy supply, resistance reduction and directional selection, and establish quantitative models incorporating dynamic contact angles, contact-angle hysteresis, precursor films, Laplace pressure differences and external-field coupling to develop predictive relationships among structural parameters, liquid properties and transport performance. On this basis, directed liquid transport on solid surfaces can advance from single-function demonstrations towards reproducible, system-integrable and scalable engineering applications only when multifunctional liquid-manipulation systems jointly consider physical mechanisms, minimum functional units, operating windows and manufacturability, with clear functional allocation and coordinated configuration of energy supply, resistance reduction and rectification.

REFERENCES

1. Buchberger G., Hischen F., Comanns P., et al. (2015). Bio-inspired microfluidic devices for passive, directional liquid transport: Model-based adaption for different materials. *Procedia Eng.* **120**:106–111. DOI:10.1016/j.proeng.2015.08.576
2. Feng J. and Rothstein J.P. (2013). One-way wicking in open micro-channels controlled by channel topography. *J. Colloid Interface Sci.* **404**:169–178. DOI:10.1016/j.jcis.2013.02.052
3. Dung Luong T. and Trung Nguyen N. (2010). Surface acoustic wave driven microfluidics – A review. *MNS* **2**:217–225. DOI:10.2174/1876402911002030217
4. Yu Z., Yun F.F., Wang Y., et al. (2017). Desert beetle-inspired superwettable patterned surfaces for water harvesting. *Small* **13**:1701403. DOI:10.1002/smll.201701403
5. Tang X., Huang J., Guo Z., et al. (2021). A combined structural and wettability gradient surface for directional droplet transport and efficient fog collection. *J. Colloid Interface Sci.* **604**:526–536. DOI:10.1016/j.jcis.2021.07.033
6. Liu L., Xie Z., Wen L., et al. (2024). Efficient collection and directional transport of condensate on superhydrophilic-hydrophobic surfaces with bioinspired hierarchical wedge-shaped channels. *Surf. Interfaces* **55**:105473. DOI:10.1016/j.surfin.2024.105473
7. Wu S., Gao S., Wang H., et al. (2023). Dropwise condensation heat transfer on vertical superhydrophobic surfaces with gradient microgrooves in humid air. *Int. J. Heat Mass Transf.* **201**:123583. DOI:10.1016/j.ijheatmasstransfer.2022.123583
8. Chen Y., Li K., Zhang S., et al. (2020). Bioinspired superwettable microspine chips with directional droplet transportation for biosensing. *ACS Nano* **14**:4654–4661. DOI:10.1021/acsnano.0c00324
9. Xie M., Qian Z., Wang X., et al. (2026). Bionic structured milli-fluidics: A review. *Chem. Rev.* **126**:1347–1407. DOI:10.1021/acs.chemrev.5c00662
10. Chaudhury M.K. and Whitesides G.M. (1992). How to make water run uphill. *Science* **256**:1539–1541. DOI:10.1126/science.256.5063.1539
11. Meng M., Chai B., Yang K., et al. (2025). Ultrafast self-transportation of multimedia droplets with a bioinspired microspine array. *Nano Lett.* **25**:3011–3019. DOI:10.1021/acs.nanolett.5c00139
12. Li J., Zhou X., Li J., et al. (2017). Topological liquid diode. *Sci. Adv.* **3**:eaao3530. DOI:10.1126/sciadv.aao3530
13. Hernández S.C., Bennett C.J.C., Junkermeier C.E., et al. (2013). Chemical gradients on graphene to drive droplet motion. *ACS Nano* **7**:4746–4755. DOI:10.1021/nn304267b
14. Zhang F., Wang Z., Liu Z., et al. (2023). Cross-hatch textured cone enables dual-mode water transport and collection. *Chem. Eng. J.* **478**:147336. DOI:10.1016/j.cej.2023.147336
15. Banuprasad T.N., Vinay T.V., Subash C.K., et al. (2017). Fast transport of water droplets over a thermo-switchable surface using rewritable wettability gradient. *ACS Appl. Mater. Interfaces* **9**:28046–28054. DOI:10.1021/acsami.7b07451
16. Lv J., Liu Y., Wei J., et al. (2016). Photocontrol of fluid slugs in liquid crystal polymer microactuators. *Nature* **537**:179–184. DOI:10.1038/nature19344
17. Cho S.K., Moon H. and Kim C.-J. (2003). Creating, transporting, cutting, and merging liquid droplets by electrowetting-based actuation for digital microfluidic circuits. *J. Microelectromech. Syst.* **12**:70–80. DOI:10.1109/JMEMS.2002.807467
18. Zhang Y., Jiang S., Hu Y., et al. (2022). Reconfigurable magnetic liquid metal robot for high-performance droplet manipulation. *Nano Lett.* **22**:2923–2933. DOI:10.1021/acs.nanolett.2c00100
19. Huan Z., Zhou J., Xie Y., et al. (2024). Automated droplet manipulation enabled by a machine-vision-assisted acoustic tweezer. *Sens. Actuators B Chem.* **418**:136352. DOI:10.1016/j.snb.2024.136352
20. Noblin X., Kofman R. and Celestini F. (2009). Ratchetlike motion of a shaken drop. *Phys. Rev. Lett.* **102**:194504. DOI:10.1103/PhysRevLett.102.194504
21. Liu C., Sun Y., Huanng J., et al. (2021). External-field-induced directional droplet transport: A review. *Adv. Colloid Interface Sci.* **295**:102502. DOI:10.1016/j.cis.2021.102502
22. Hou L., Liu X., Ge X., et al. (2023). Designing of anisotropic gradient surfaces for directional liquid transport: Fundamentals, construction, and applications. *The Innovation* **4**:100508. DOI:10.1016/j.xinn.2023.100508
23. Li C., Kim B., Yoon J., et al. (2024). Advances in directional wetting surfaces for enhanced fluid control: A comprehensive review. *Adv. Funct. Mater.* **34**:2308265. DOI:10.1002/adfm.202308265
24. Bai H., Zhao T. and Cao M. (2025). Interfacial fluid manipulation with bioinspired strategies: Special wettability and asymmetric structures. *Chem. Soc. Rev.* **54**:1733–1784. DOI:10.1039/D4CS01073F
25. Miao J., Zhang Y., Wang L., et al. (2026). Bioinspired adaptive surfaces for intelligent liquid manipulation: Progressing from passive and active to hybrid strategies. *Adv. Mater.* e74360. DOI:10.1002/adma.74360.
26. Sun S., Wang L. and Zhang Y. (2026). Structure-enabled liquid manipulation: Bioinspired control across all dimensions. *Lab Chip* **26**:1547–1565. DOI:10.1039/D5LC00828J
27. Duncombe T.A., Erdem E.Y., Shastry A., et al. (2012). Controlling liquid drops with texture ratchets. *Adv. Mater.* **24**:1545–1550. DOI:10.1002/adma.201104446
28. Zhang C., Zhang H., Wang C., et al. (2025). Controllable lubricant-infused wrinkled surface for light-manipulated droplet climbing/pinning on inclined surfaces. *J. Colloid Interface Sci.* **690**:137367. DOI:10.1016/j.jcis.2025.137367
29. Ichimura K., Oh S.-K. and Nakagawa M. (2000). Light-driven motion of liquids on a photoresponsive surface. *Science* **288**:1624–1626. DOI:10.1126/science.288.5471.1624
30. Gao C., Wang L., Lin Y., et al. (2018). Droplets manipulated on photothermal organogel surfaces. *Adv. Funct. Mater.* **28**:1803072. DOI:10.1002/adfm.201803072
31. Ye W.-Q., Wei Y.-Y., Wang D.-N., et al. (2021). A digital microfluidic platform based on a near-infrared light-responsive shape-memory micropillar array. *Lab Chip* **21**:1131–1138. DOI:10.1039/D0LC01324B
32. Nasirimarekani V., Benito-Lopez F. and Basabe-Desmonts L. (2021). Tunable superparamagnetic ring (tSPRing) for droplet manipulation. *Adv. Funct. Mater.* **31**:2100178. DOI:10.1002/adfm.202100178
33. Shao K., Jiang S., Hu Y., et al. (2022). Bioinspired lubricated slippery magnetic responsive microplate array for high performance multi-substance transport. *Adv. Funct. Mater.* **32**:2205831. DOI:10.1002/adfm.202205831
34. Ben S., Zhou T., Ma H., et al. (2019). Multifunctional magnetocontrollable superwettable-microcilia surface for directional droplet manipulation. *Adv. Sci.* **6**:1900834. DOI:10.1002/advs.201900834
35. Seo K.S., Wi R., Im S.G., et al. (2013). A superhydrophobic magnetic elastomer actuator for droplet motion control. *Polym. Adv. Technol.* **24**:1075–1080. DOI:10.1002/pat.3190
36. Yang L., Li W., Lian J., et al. (2024). Selective directional liquid transport on shoot surfaces of Crassula muscosa. *Science* **384**:1344–1349. DOI:10.1126/science.adk4180
37. Dai S., Zhang H., Liu Y., et al. (2026). Bulk-cusp microstructure for controllable multi-directional liquid spreading. *Nat. Commun.* **17**:1519. DOI:10.1038/s41467-025-68237-8
38. Young T. (1805). An essay on the cohesion of fluids. *Philos. Trans. R. Soc. Lond.* **95**:65–87.
39. Gao S. and Liu H. (2010). Capillary mechanics (Science Press). (in Chinese).
40. Marangoni C. (1871). Ueber die Ausbreitung der Tropfen einer Flüssigkeit auf der Oberfläche einer anderen. *Ann. Phys.* **219**:337–354. DOI:10.1002/andp.18712190702
41. Li D. (2008). Encyclopedia of microfluidics and nanofluidics (Springer).
42. Brochard F. (1989). Motions of droplets on solid surfaces induced by chemical or thermal gradients. *Langmuir* **5**:432–438. DOI:10.1021/la00086a025
43. Furmidge C.G.L. (1962). Studies at phase interfaces. *I. The sliding of liquid drops on solid surfaces and a theory for spray retention. J. Colloid Sci.* **17**:309–324. DOI:10.1016/0095-8522(62)90011-9
44. Xin B. and Hao J. (2010). Reversibly switchable wettability. *Chem. Soc. Rev.* **39**:769–782. DOI:10.1039/B913622C
45. Liu C., Sun J., Li J., et al. (2017). Long-range spontaneous droplet self-propulsion on wettability gradient surfaces. *Sci. Rep.* **7**:7552. DOI:10.1038/s41598-017-07867-5
46. Lee J., Moon H., Fowler J., et al. (2002). Electrowetting and electrowetting-on-dielectric for microscale liquid handling. *Sens. Actuators A Phys.* **95**:259–268. DOI:10.1016/S0924-4247(01)00734-8

47. Tian D., Zhang N., Zheng X., et al. (2016). Fast responsive and controllable liquid transport on a magnetic fluid/nanoarray composite interface. *ACS Nano* **10**:6220–6226. DOI:10.1021/acsnano.6b02318
48. Fox H.W. and Zisman W.A. (1952). The spreading of liquids on low-energy surfaces. *II. Modified tetrafluoroethylene polymers. J. Colloid Sci.* **7**:109–121. DOI:10.1016/0095-8522(52)90054-8
49. Shafrin E.G. and Zisman W.A. (1960). Constitutive relations in the wetting of low energy surfaces and the theory of the retraction method of preparing monolayers. *J. Phys. Chem.* **64**:519–524.
50. Bain C.D., Burnett-Hall G.D. and Montgomerie R.R. (1994). Rapid motion of liquid drops. *Nature* **372**:414–415. DOI:10.1038/372414a0
51. Zamuruyev K.O., Bardaweel H.K., Carron C.J., et al. (2014). Continuous droplet removal upon dropwise condensation of humid air on a hydrophobic micropatterned surface. *Langmuir* **30**:10133–10142. DOI:10.1021/la5004462
52. Cassie A.B.D. and Baxter S. (1944). Wettability of porous surfaces. *Trans. Faraday Soc.* **40**:546. DOI:10.1039/tf9444000546
53. Quéré D. (2008). Wetting and roughness. *Annu. Rev. Mater. Res.* **38**:71–99. DOI:10.1146/annurev.matsci.38.060407.132434
54. Wenzel R.N. (1936). Resistance of solid surfaces to wetting by water. *Ind. Eng. Chem.* **28**:988–994. DOI:10.1021/ie50320a024
55. Diaz M.E., Savage M.D. and Cerro R.L. (2017). The effect of temperature on contact angles and wetting transitions for n-alkanes on PTFE. *J. Colloid Interface Sci.* **503**:159–167. DOI:10.1016/j.jcis.2017.05.003
56. Song J.-W. and Fan L.-W. (2022). Unraveling the synergistic effects of solid surface material and temperature on the contact angle of water under an elevated pressure: An experimental study. *J. Colloid Interface Sci.* **605**:163–172. DOI:10.1016/j.jcis.2021.07.042
57. Zhu L., Zhang Z., Li M., et al. (2010). Contact angle and action of adhesion between epoxy resin and fibers at processing temperatures. *Acta Mater. Compos. Sin.* **27**:41–46. (in Chinese).
58. Sun J., Yang H., Wang M., et al. (2011). Influence analysis of contact angle between polyester resin and fibers under different temperature. *J. Chongqing Univ. Technol. (Nat. Sci.)* **25**:61–64,85. DOI:10.3969/j.issn.1674-8425-B.2011.04.012
59. Song J.-W. and Fan L.-W. (2021). Temperature dependence of the contact angle of water: A review of research progress, theoretical understanding, and implications for boiling heat transfer. *Adv. Colloid Interface Sci.* **288**:102339. DOI:10.1016/j.cis.2020.102339
60. Wang J., Gao W., Zhang H., et al. (2018). Programmable wettability on photocontrolled graphene film. *Sci. Adv.* **4**:eaat7392. DOI:10.1126/sciadv.aat7392
61. Brzoska J.B., Brochard-Wyart F. and Rondelez F. (1993). Motions of droplets on hydrophobic model surfaces induced by thermal gradients. *Langmuir* **9**:2220–2224. DOI:10.1021/la00032a052
62. Jochum F.D. and Theato P. (2013). Temperature- and light-responsive smart polymer materials. *Chem. Soc. Rev.* **42**:7468–7483. DOI:10.1039/C2CS35191A
63. Wang R., Hashimoto K., Fujishima A., et al. (1997). Light-induced amphiphilic surfaces. *Nature* **388**:431–432. DOI:10.1038/41233
64. Wang S., Song Y. and Jiang L. (2007). Photoresponsive surfaces with controllable wettability. *J. Photochem. Photobiol. C Photochem. Rev.* **8**:18–29. DOI:10.1016/j.jphotochemrev.2007.03.001
65. Bernà J., Leigh D.A., Lubomska M., et al. (2005). Macroscopic transport by synthetic molecular machines. *Nat. Mater.* **4**:704–710. DOI:10.1038/nmat1455
66. Beni G. and Hackwood S. (1981). Electro-wetting displays. *Appl. Phys. Lett.* **38**:207–209. DOI:10.1063/1.92322
67. Vallet M., Berge B. and Vovelle L. (1996). Electrowetting of water and aqueous solutions on poly(ethylene terephthalate) insulating films. *Polymer* **37**:2465–2470. DOI:10.1016/0032-3861(96)85360-2
68. Orejon D., Sefiane K. and Shanahan M.E.R. (2013). Young-Lippmann equation revisited for nano-suspensions. *Appl. Phys. Lett.* **102**:201601. DOI:10.1063/1.4807120
69. Cooney C.G., Chen C.-Y., Emerling M.R., et al. (2006). Electrowetting droplet microfluidics on a single planar surface. *Microfluid. Nanofluid.* **2**:435–446. DOI:10.1007/s10404-006-0085-8
70. Chiou P.-Y., Chang Z. and Wu M.C. (2008). Droplet manipulation with light on optoelectrowetting device. *J. Microelectromech. Syst.* **17**:133–138. DOI:10.1109/JMEMS.2007.904336
71. Liu M., Chen R., Yuan J., et al. (2025). Multimodal splitting and reciprocating transport of droplets on a reprogrammable functional surface. *Langmuir* **41**:4176–4184. DOI:10.1021/acs.langmuir.4c04726
72. Gallardo B.S., Gupta V.K., Eagerton F.D., et al. (1999). Electrochemical principles for active control of liquids on submillimeter scales. *Science* **283**:57–60. DOI:10.1126/science.283.5398.57
73. Wang W. (2021). Research on the fabrication of Marangoni actuators and their multi-field coupled manipulation. Doctoral dissertation. (in Chinese).
74. Weislogel M.M. (1997). Steady spontaneous capillary flow in partially coated tubes. *AIChE J.* **43**:645–654. DOI:10.1002/aic.690430310
75. Hauksbee F. (1711). III. *An account of an experiment touching the direction of a drop of oil of oranges, between two glass planes, towards any side of them that is nearest press'd together. Philos. Trans. R. Soc. Lond.* **27**:395–396. DOI:10.1098/rstl.1710.0036
76. Lorenceau É. and Quéré D. (2004). Drops on a conical wire. *J. Fluid Mech.* **510**:29–45. DOI:10.1017/S0022112004009152
77. Prakash M., Quéré D. and Bush J.W.M. (2008). Surface tension transport of prey by feeding shorebirds: The capillary ratchet. *Science* **320**:931–934. DOI:10.1126/science.1156023
78. Ma X., Cao M., Teng C., et al. (2015). Bio-inspired humidity responsive switch for directional water droplet delivery. *J. Mater. Chem. A* **3**:15540–15545. DOI:10.1039/C5TA03309H
79. Li M., Lu Y., Wang Y., et al. (2024). Synergistically biomimetic platform that enables droplets to be self-propelled. *Int. J. Extrem. Manuf.* **6**:055503. DOI:10.1088/2631-7990/ad5bc4
80. Luo C. (2015). Theoretical exploration of barrel-shaped drops on cactus spines. *Langmuir* **31**:11809–11813. DOI:10.1021/acs.langmuir.5b03600
81. Zheng Y., Bai H., Huang Z., et al. (2010). Directional water collection on wetted spider silk. *Nature* **463**:640–643. DOI:10.1038/nature08729
82. Ju J., Bai H., Zheng Y., et al. (2012). A multi-structural and multi-functional integrated fog collection system in cactus. *Nat. Commun.* **3**:1247. DOI:10.1038/ncomms2253
83. Chen H., Ran T., Gan Y., et al. (2018). Ultrafast water harvesting and transport in hierarchical microchannels. *Nat. Mater.* **17**:935–942. DOI:10.1038/s41563-018-0171-9
84. Pan Z., Pitt W.G., Zhang Y., et al. (2016). The upside-down water collection system of Syntrichia caninervis. *Nat. Plants* **2**:16076. DOI:10.1038/nplants.2016.76
85. Chen D., Niu S., Zhang J., et al. (2018). Superfast liquid transfer strategy through sliding on a liquid membrane inspired from scorpion setae. *Adv. Mater. Interfaces* **5**:1800802. DOI:10.1002/admi.201800802
86. Ju J., Xiao K., Yao X., et al. (2013). Bioinspired conical copper wire with gradient wettability for continuous and efficient fog collection. *Adv. Mater.* **25**:5937–5942. DOI:10.1002/adma.201301876
87. Lei W., Hou G., Liu M., et al. (2018). High-speed transport of liquid droplets in magnetic tubular microactuators. *Sci. Adv.* **4**:eaau8767. DOI:10.1126/sciadv.aau8767
88. Renvoisé P., Bush J.W.M., Prakash M., et al. (2009). Drop propulsion in tapered tubes. *EPL* **86**:64003. DOI:10.1209/0295-5075/86/64003
89. Liu J.L., Xia R., Li B.W., et al. (2007). Directional motion of droplets in a conical tube or on a conical fibre. *Chin. Phys. Lett.* **24**:3210–3213. DOI:10.1088/0256-307X/24/11/052
90. Dudukovic N.A., Fong E.J., Gemeda H.B., et al. (2021). Cellular fluidics. *Nature* **595**:58–65. DOI:10.1038/s41586-021-03603-2
91. Guo H.A., Maheshwari S., Patel M.S., et al. (2019). Droplet actuation on superhydrophobic substrates via electric field gradients. *Appl. Phys. Lett.* **114**:113702. DOI:10.1063/1.5080241
92. Wang Y., Gong J., Li X., et al. (2025). Study on directionally propelled droplet based on the piezoelectric-acoustic streaming effect. *CIESC J.* **76**:181. DOI:10.11949/0438-1157.20241382
93. Wu X., Gong J., Gao T., et al. (2024). Experimental study on dynamic wetting behavior of liquid droplets on the aluminum surfaces excited by ultrasonic waves. *Appl. Therm. Eng.* **248**:123209. DOI:10.1016/j.applthermaleng.2024.123209
94. Nijith R., Arjunan P., Thampi B.S.G., et al. (2026). Experimental investigation on transport of self-propelled Leidenfrost droplet on herringbone and helical ratchet surfaces. In Shine S.R. and Sunil Kumar S. (eds). Advances in aerospace and energy, Volume II (Springer Nature Singapore), pp:153–162.
95. Jones T.B. (2005). Electromechanics of particles (Cambridge University Press).
96. Ahmed R., Hsu D., Bailey C., et al. (2004). Dispensing picoliter droplets using dielectrophoretic (DEP) microactuation. *Microscale Thermophys. Eng.* **8**:271–283. DOI:10.1080/10893950490477572
97. Ahmed R. and Jones T.B. (2006). Dispensing picoliter droplets on substrates using dielectrophoresis. *J. Electrostat.* **64**:543–549. DOI:10.1016/j.elstat.2005.10.008
98. Mertaniemi H., Jokinen V., Sainiemi L., et al. (2011). Superhydrophobic tracks for low-friction, guided transport of water droplets. *Adv. Mater.* **23**:2911–2914. DOI:10.1002/adma.201100461
99. Sun Q., Wang D., Li Y., et al. (2019). Surface charge printing for programmed droplet transport. *Nat. Mater.* **18**:936–941. DOI:10.1038/s41563-019-0440-2
100. Wang F., Liu M., Liu C., et al. (2023). Light control of droplets on photo-induced charged surfaces. *Natl. Sci. Rev.* **10**:nwac164. DOI:10.1093/nsr/nwac164
101. Fan X., Dong X., Karacakol A.C., et al. (2020). Reconfigurable multifunctional ferrofluid droplet robots. *Proc. Natl. Acad. Sci. U.S.A.* **117**:27916–27926. DOI:10.1073/pnas.2016388117
102. Khalil K.S., Mahmoudi S.R., Abu-dheir N., et al. (2014). Active surfaces: Ferrofluid-impregnated surfaces for active manipulation of droplets. *Appl. Phys. Lett.* **105**:041604. DOI:10.1063/1.4891439
103. Li X., Li S., Lu Y., et al. (2020). Programmable digital liquid metal droplets in reconfigurable magnetic fields. *ACS Appl. Mater. Interfaces* **12**:37670–37679. DOI:10.1021/acsami.0c08179
104. He X., Ni M., Wu J., et al. (2021). Hard-magnetic liquid metal droplets with excellent magnetic field dependent mobility and elasticity. *J. Mater. Sci. Technol.* **92**:60–68. DOI:10.1016/j.jmst.2021.04.004

105. Li A., Li H., Li Z., et al. (2020). Programmable droplet manipulation by a magnetic-actuated robot. *Sci. Adv.* **6**:eaay5808. DOI:10.1126/sciadv.aay5808
106. Wang J., Zhu Z., Liu P., et al. (2021). Magneto-responsive shutter for on-demand droplet manipulation. *Adv. Sci.* **8**:2103182. DOI:10.1002/advs.202103182
107. Das P.Kr., Snider A.D. and Bhethanabotla V.R. (2019). Acoustothermal heating in surface acoustic wave driven microchannel flow. *Phys. Fluids* **31**:106106. DOI:10.1063/1.5121307
108. Fasano M., Li Y., Diez J.A., et al. (2025). Modelling the dynamics of an oil drop driven by a surface acoustic wave in the underlying substrate. *J. Fluid Mech.* **1022**:A49. DOI:10.1017/jfm.2025.10802
109. Zhang S.P., Lata J., Chen C., et al. (2018). Digital acoustofluidics enables contactless and programmable liquid handling. *Nat. Commun.* **9**:2928. DOI:10.1038/s41467-018-05297-z
110. Barmatz M. and Collas P. (1985). Acoustic radiation potential on a sphere in plane, cylindrical, and spherical standing wave fields. *J. Acoust. Soc. Am.* **77**:928–945. DOI:10.1121/1.392061
111. Hasegawa K. (2023). Contactless manipulation of levitated droplets driven by acoustic fields. *Jpn. J. Multiph. Flow* **37**:29–36. DOI:10.3811/jjmf.2023.T004
112. Zang D., Yu Y., Chen Z., et al. (2017). Acoustic levitation of liquid drops: Dynamics, manipulation and phase transitions. *Adv. Colloid Interface Sci.* **243**:77–85. DOI:10.1016/j.cis.2017.03.003
113. Linke H., Alemán B.J., Melling L.D., et al. (2006). Self-propelled Leidenfrost droplets. *Phys. Rev. Lett.* **96**:154502. DOI:10.1103/PhysRevLett.96.154502
114. Mrinal M., Wang X. and Luo C. (2017). Self-rotation-induced propulsion of a Leidenfrost drop on a ratchet. *Langmuir* **33**:6307–6313. DOI:10.1021/acs.langmuir.7b01420
115. Li B., Jiang L., Li X., et al. (2024). Self-propelled Leidenfrost droplets on femtosecond-laser-induced surface with periodic hydrophobicity gradient. *Int. J. Extrem. Manuf.* **6**:025502. DOI:10.1088/2631-7990/ad18fb
116. Scortesse J., Manceau J.F. and Bastien F. (2002). Interaction between a liquid layer and vibrating plates: Application to the displacement of liquid droplets. *J. Sound Vib.* **254**:927–938. DOI:10.1006/jsvi.2001.4137
117. Alzuaga S., Manceau J.-F. and Bastien F. (2005). Motion of droplets on solid surface using acoustic radiation pressure. *J. Sound Vib.* **282**:151–162. DOI:10.1016/j.jsv.2004.02.020
118. Chen X. and Lal A. (2005). Surface liquid droplet motion on silicon ultrasonic horn actuators. In Proceedings of the IEEE Ultrasonics Symposium (IEEE), pp:1032–1035.
119. Daniel S., Chaudhury M.K. and De Gennes P.-G. (2005). Vibration-actuated drop motion on surfaces for batch microfluidic processes. *Langmuir* **21**:4240–4248. DOI:10.1021/la046886s
120. Brunet P., Eggers J. and Deegan R.D. (2009). Motion of a drop driven by substrate vibrations. *Eur. Phys. J. Spec. Top.* **166**:11–14. DOI:10.1140/epjst/e2009-00870-6
121. Sartori P., Quagliati D., Varagnolo S., et al. (2015). Drop motion induced by vertical vibrations. *New J. Phys.* **17**:113017. DOI:10.1088/1367-2630/17/11/113017
122. Leidenfrost J.G. (1756). A tract about some qualities of common water (Herman Overnius).
123. Shine S.R. and Sunil Kumar S. (eds) (2026). Advances in aerospace and energy, Volume II: Proceedings of International Conference on Advances in Aerospace and Energy (IAES 2024) (Springer Nature Singapore).
124. Gavrilyuk S. and Gouin H. (2022). Theoretical model of the Leidenfrost temperature. *Phys. Rev. E* **106**:055102. DOI:10.1103/PhysRevE.106.055102
125. Dupeux G., Le Merrer M., Lagubeau G., et al. (2011). Viscous mechanism for Leidenfrost propulsion on a ratchet. *EPL* **96**:58001. DOI:10.1209/0295-5075/96/58001
126. Würger A. (2011). Leidenfrost gas ratchets driven by thermal creep. *Phys. Rev. Lett.* **107**:164502. DOI:10.1103/PhysRevLett.107.164502
127. Lagubeau G., Le Merrer M., Clanet C., et al. (2011). Leidenfrost on a ratchet. *Nat. Phys.* **7**:395–398. DOI:10.1038/nphys1925
128. Jo D. (2023). Motion of Leidenfrost self-propelled droplets on ratchet in low- and high-temperature regimes. *J. Mech. Sci. Technol.* **37**:5425–5430. DOI:10.1007/s12206-023-0941-4
129. Jia Z., Chen M. and Zhu H. (2017). Reversible self-propelled Leidenfrost droplets on ratchet surfaces. *Appl. Phys. Lett.* **110**:091603. DOI:10.1063/1.4976748
130. Cao G., Huang S., Li M., et al. (2021). Advances in research on directional movement of droplets on wetted anisotropic surfaces. *J. Exp. Fluid Mech.* **35**:67–85. (in Chinese).
131. Wu D., Wang J., Wu S., et al. (2011). Three-level biomimetic rice-leaf surfaces with controllable anisotropic sliding. *Adv. Funct. Mater.* **21**:2927–2932. DOI:10.1002/adfm.201002733
132. Chen H., Zhang P., Zhang L., et al. (2016). Continuous directional water transport on the peristome surface of Nepenthes alata. *Nature* **532**:85–89. DOI:10.1038/nature17189
133. Concus P. and Finn R. (1969). On the behavior of a capillary surface in a wedge. *Proc. Natl. Acad. Sci. U.S.A.* **63**:292–299. DOI:10.1073/pnas.63.2.292
134. Oliver J.F., Huh C. and Mason S.G. (1977). Resistance to spreading of liquids by sharp edges. *J. Colloid Interface Sci.* **59**:568–581. DOI:10.1016/0021-9797(77)90052-2
135. Feng S., Zhu P., Zheng H., et al. (2021). Three-dimensional capillary ratchet-induced liquid directional steering. *Science* **373**:1344–1348. DOI:10.1126/science.abg7552
136. Feng S., Delannoy J., Malod A., et al. (2020). Tip-induced flipping of droplets on Janus pillars: From local reconfiguration to global transport. *Sci. Adv.* **6**:eabb4540. DOI:10.1126/sciadv.abb4540
137. Comanns P., Effertz C., Hischen F., et al. (2011). Moisture harvesting and water transport through specialized micro-structures on the integument of lizards. *Beilstein J. Nanotechnol.* **2**:204–214. DOI:10.3762/bjnano.2.24
138. Liu C., Ju J., Zheng Y., et al. (2014). Asymmetric ratchet effect for directional transport of fog drops on static and dynamic butterfly wings. *ACS Nano* **8**:1321–1329. DOI:10.1021/nn404761q
139. Li C., Dai H., Gao C., et al. (2019). Bioinspired inner microstructured tube controlled capillary rise. *Proc. Natl. Acad. Sci. U.S.A.* **116**:12704–12709. DOI:10.1073/pnas.1821493116
140. Li J., Zhou X., Tao R., et al. (2021). Directional liquid transport from the cold region to the hot region on a topological surface. *Langmuir* **37**:5059–5065. DOI:10.1021/acs.langmuir.1c00627
141. Sun J., Qin X., Song Y., et al. (2023). Selective liquid directional steering enabled by dual-scale reentrant ratchets. *Int. J. Extrem. Manuf.* **5**:025504. DOI:10.1088/2631-7990/acccbc
142. Miao J. and Tsang A.C.H. (2025). Smart directional liquid manipulation on curvature-ratchet surfaces. *ACS Nano* **19**:5829–5838. DOI:10.1021/acsnano.4c18229
143. Sun S., Zhang Y., Wu S., et al. (2024). In situ multi-directional liquid manipulation enabled by 3D asymmetric Fang-structured surface. *Adv. Mater.* **36**:2407034. DOI:10.1002/adma.202407034
144. Wu S., Sun S., Ye J., et al. (2025). Capillary-driven 3D open fluidic networks for versatile continuous flow manipulation. *Adv. Mater.* **37**:2503840. DOI:10.1002/adma.202503840
145. Malvadkar N.A., Hancock M.J., Sekeroglu K., et al. (2010). An engineered anisotropic nanofilm with unidirectional wetting properties. *Nat. Mater.* **9**:1023–1028. DOI:10.1038/nmat2864
146. Duncombe T.A., Parsons J.F. and Böhringer K.F. (2012). Directed drop transport rectified from orthogonal vibrations via a flat wetting barrier ratchet. *Langmuir* **28**:13765–13770. DOI:10.1021/la3024309
147. Son C., Yang Z., Kim S., et al. (2023). Bidirectional droplet manipulation on magnetically actuated superhydrophobic ratchet surfaces. *ACS Nano* **17**:23702–23713. DOI:10.1021/acsnano.3c07360
148. Chu K.-H., Xiao R. and Wang E.N. (2010). Uni-directional liquid spreading on asymmetric nanostructured surfaces. *Nat. Mater.* **9**:413–417. DOI:10.1038/nmat2726
149. Miao J. and Tsang A.C.H. (2024). Reconfigurability-encoded hierarchical rectifiers for versatile 3D liquid manipulation. *Adv. Sci.* **11**:2405641. DOI:10.1002/advs.202405641
150. Miao J., Li J. and Tsang A.C.H. (2025). Competition and synergy in programmable open microfluidics: Thermal fields vs structural heterogeneities. *Nano Lett.* **25**:12495–12502. DOI:10.1021/acs.nanolett.5c02353

FUNDING AND ACKNOWLEDGMENTS

This study was supported by the independent research project of the Innovation Research Foundation of National University of Defense Technology (NUDT) (ZK23-41, 26-ZZCX-JDZ-49) and Innovation Research Foundation of College of Aerospace Science and Engineering at NUDT.

AUTHOR CONTRIBUTIONS

Yong Tian: Conceptualization, Investigation, Data curation, Formal analysis, Visualization, Writing – original draft. Xin Song: Supervision, Project administration, Writing – review & editing. Qianghui Xu: Conceptualization, Formal analysis, Visualization, Supervision, Writing – original draft, Writing – review & editing, Project administration. Bingxiao Du: Formal analysis, Funding acquisition, Writing – review & editing. Jialin Liang: Investigation, Writing – review & editing. Zhenzhen Wang: Investigation, Writing – review & editing. Yong Zhao: Formal analysis, Writing – review & editing. Jun Shen: Formal analysis, Writing – review & editing.

DECLARATION OF INTERESTS

Jun Shen is an Editorial Board member of The Innovation Energy and was blinded from reviewing or making final decisions on the manuscript. Peer review was handled independently of this member and their research group. The other authors declare no conflicts of interest.

DATA AND CODE AVAILABILITY

Data are available from the corresponding author upon reasonable request.

SUPPLEMENTAL INFORMATION

It can be found online at https://doi.org/10.59717/j.xinn-energy.2026.100200